Terahertz waves: a tool for condensed matter, the life sciences and astronomy

Yukio Kawano

Taylor & Francis
Taylor & Francis Group

Terahertz waves: a tool for condensed matter, the life sciences and astronomy

Yukio Kawano*

Quantum Nanoelectronics Research Center and Department of Physical Electronics, Tokyo Institute of Technology, Meguro-ku, Tokyo 152-8552, Japan

In the wide range of the electromagnetic wave spectrum, the terahertz (THz) frequency region has for a long time been an unexplored region and its technological development has been left behind. Nowadays, however, science and technology based on THz electromagnetic waves have been increasingly progressing and are still growing. In the THz region, both features of 'wave' and 'light' appear, enabling the manipulation of the THz wave from both approaches of electronics and optics/photonics. From the viewpoint of research targets, THz technology is expected to be the key for unlocking mysteries behind quantum effects in condensed-matter physics, life activities in biology, and the birth of the celestial bodies in astronomy. In addition to such fundamental sciences, THz spectroscopy and imaging can be used as a powerful tool for nondestructive remote inspection in industrial and medical fields. In this article I review cutting-edge technologies of THz sensing, imaging and spectroscopy, and describe how effectively the THz measurements are applied to various researches.

Keywords: terahertz; single photon detector; near-field imaging; time-domain spectroscopy; carbon nanotube; graphene

1. Introduction

Since the establishment of the Maxwell equation and the discovery of the electromagnetic wave, researchers have been devoted to investigate the inherent nature of the electromagnetic wave and to develop many technologies. One of the important findings obtained by the Maxwell equation is that radio wave, microwave, infrared (IR) light, visible light, ultraviolet light, and X-ray are all a type of electromagnetic wave and that these waves and lights are comprehensively classified with their frequencies. Another important aspect was revealed by the birth of quantum mechanics. The electromagnetic wave has a dual feature of 'wave' and 'particle' and the particle of the electromagnetic wave is called a 'photon'.

Nowadays, there are two approaches for studying and producing technologies based on the electromagnetic wave: electronics and optics/photonics. The electronics is mainly understood in terms of an electrical circuit. High frequency electronics technology has provided radar, radio, television, cellular phones, and so on. From the approach based on optics/photonics, optical communication, light-emitting diode, endoscope, etc. have been produced. In either case, these technologies have brought much change in human life.

The terahertz (THz, 10^{12} Hz) frequency region is located between the microwave region and the infrared (IR) light region (Figure 1). Formerly, this region was merely studied by a small number of researchers in a few limited fields,

such as chemical spectroscopy, astronomy, and solid-state physics. However, THz technology is now in strong demand in a large variety of fields, ranging from basic sciences such as biochemical spectroscopy, astronomy, and condensed-matter physics to practical applications such as high-capacity communication, medicine, agriculture, and security [1,2]. Why do the THz waves attract so much interest? Since the THz frequency is located in the 'wave' and 'light' regions, the THz electromagnetic wave has both features and can be controlled with either electrical or optical components such as waveguide, antenna, mirror, and lens. (Therefore we can call the THz electromagnetic wave either 'THz wave' and/or 'THz light'. Throughout this article I use the THz wave to prevent confusion.)

In terms of THz photons, the corresponding photon energy, 1–100 meV is in the important energy region for a variety of materials and molecules. These features allow diverse applications of imaging and spectroscopy with this frequency band. Figure 2 displays several examples of applications of the THz imaging measurements. For the measurements shown here THz waves are irradiated onto objects and the intensity distribution of THz reflection or transmission is imaged. Furthermore, simultaneous measurements with frequency spectra provide more explicit information about physical/chemical properties. The THz imaging and spectroscopy therefore can be used for nondestructive remote inspection. Compared to X-ray imaging,

*Email: kawano@pe.titech.ac.jp

Figure 1. Chart of the electromagnetic wave spectrum.

the THz wave is less harmful and does not cause much damage, because the photon energy is far lower. In addition to industrial and medical applications, THz technology is also of much interest in basic sciences. For example, in astronomy, condensed-matter physics and biochemistry, the detection of very weak THz radiation from interstellar matter in space, electrons in materials and bio-molecules is expected to unlock mysteries behind the early universe, quantum effects in condensed-matters and life activities, respectively.

In the THz region, however, even basic components like detector and source have not been fully established, compared to the other frequency regions that are technically mature. The reasons are (i) that the THz frequency is too high to be handled by conventional high frequency semiconductor technology and (ii) that the photon energy of the THz wave is much lower than the band gap energy of semiconductors (typically the order of eV). Therefore, the THz wave is not easily controlled and manipulated either by electronics or optics/photonics. Regarding imaging technology, the THz wave also has an intrinsic problem of low spatial resolution (typically the order of mm), which results from the much longer wavelength of the THz wave than that of the visible light.

However, recent advance in materials, device structures, laser systems, etc. is opening up new opportunities to overcome such difficulties. In particular, the use of nanostructured devices based on superconductors, semiconductors, and carbon nanotubes and the application of advanced laser technologies like femto-second pulse lasers have led to significant progress in detection sensitivity, spatial resolution and frequency bandwidth, expanding the applications of THz technology. In this article, I give an overview of the current status of the THz sensing, imaging and spectroscopy, and show the availability and usefulness of THz technology in visualising and analysing various objects.

2. THz sensing

2.1. General overview

As emphasised in the introduction, compared to the detection in other frequency regions, the difficulty in sensing the THz wave originates from the fact that the frequency is too high in terms of high frequency electronics and the fact that the photon energy is much lower than that of the visible light. This means that the development of high-performance THz detectors requires new device concepts beyond conventional electronics and optics/photonics.

Generally, THz detection falls into three types: bolometric (thermal) detection, wave detection, and quantum detection. In these respective types of detection, the THz wave is regarded as 'heat', 'wave', and 'photon'. In this section, I give an overview of various THz detectors and briefly discuss their advantages and disadvantages.

2.1.1. Bolometric (thermal) detection

This type of detector utilises temperature rise via THz absorption. As the crystal temperature of the detector decreases, the detection sensitivity is improved, but the detection speed becomes low. A typical time constant is of the order of ms below 4 K. The detected signal is usually the resistance change arising from the rise in the crystal temperature induced by the THz absorption. Representative devices of this type are pyroelectric detectors at room temperature, Si bolometers below 4.2 K, and superconducting hot electron bolometers below 4.2 K [3]. The superconducting hot electron bolometer uses a steep resistance change near the critical temperature and has the advantage of high speed detection (ns–ps) even at the low temperature [3].

Another type of readout mechanism is to measure gas pressure via thermal expansion (Golay cell detector). Since all the detectors based on the bolometric detection respond to electromagnetic waves in a wide frequency region, an appropriate frequency cut-off filter is necessary.

2.1.2. Wave detection

This type of detector senses the THz electromagnetic wave as a high-frequency 'wave'. As a representative device, a Schottky-barrier diode detector is well known and is commercially available. The advantages of this detector are high speed detection with the time constant of $\sim$ns and room-temperature operation. This detector is often used in sub-THz regions, because the sensitivity becomes low with increasing frequency of the incident THz wave.

As well, there are photoconductive antennas, electro-optic devices, and frequency mixers for heterodyne detection. The two former are used in THz time-domain spectroscopy (TDS). Though these detectors work at room temperature, their operation requires an expensive femto-second pulse laser. I will explain details of the TDS in Section 4. THz spectroscopy. The frequency mixer measures a beat signal corresponding to frequency difference with a local oscillator. Superconductors, semiconductor heterostructures, carbon nanotubes (CNTs), etc. are used as materials for the frequency mixer. This type of detector is often used in the fields of astronomy and environmental science.
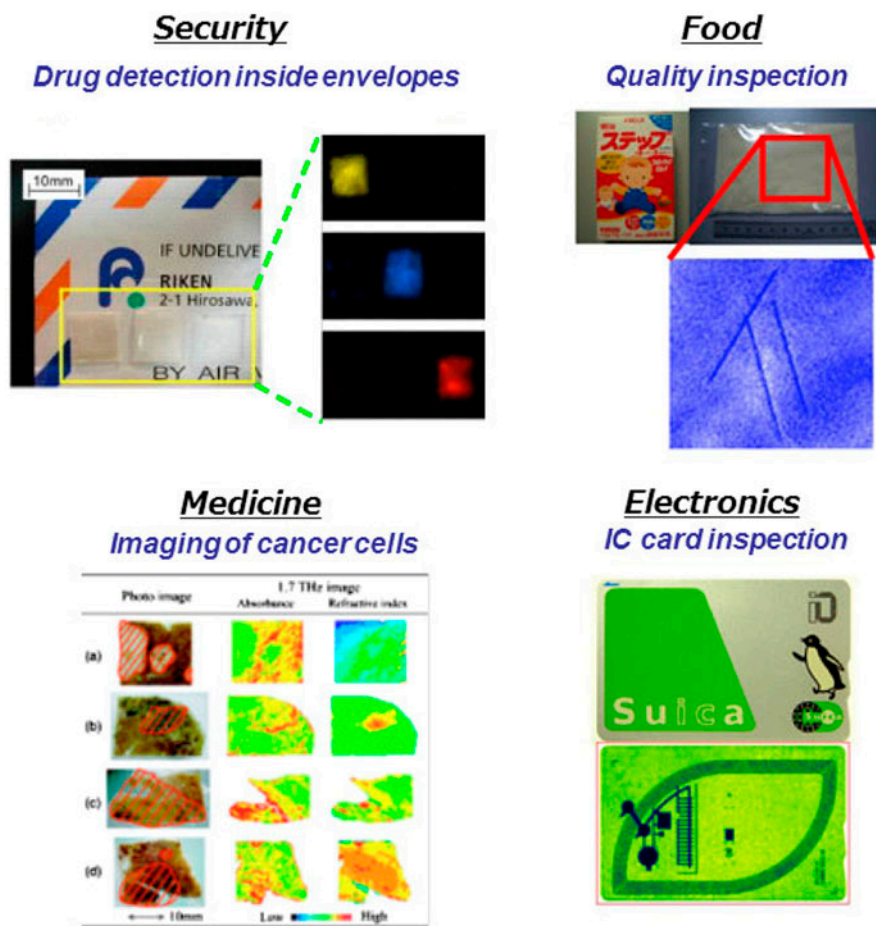
Security
Drug detection inside envelopes

Food
Quality inspection

Medicine
Imaging of cancer cells

Electronics
IC card inspection

Figure 2. Applications of the THz imaging and spectroscopy. Reprinted with permission from: Kawase et al., Opt. Express 11 (2003), 2549 for security, Nakajima et al., Appl. Phys. Lett. 90 (2007), 041102 for medicine, Ariyoshi et al., Appl. Phys. Lett. 88 (2006), 203503 for food, and Dobroiu et al., Appl. Opt. 43 (2004), 5367 for electronics.

2.1.3. *Quantum detection*

In contrast to the wave detection, this type of detector senses 'photons' of the THz wave. Solid-state devices made of materials like superconductors and semiconductors usually have energy level spacing corresponding to the THz photon energy (1–100 meV), for example, the energy gap of a superconductor, the impurity level of a semiconductor, or the energy level spacing due to quantum electron confinement of semiconductors. It follows that when these devices are illuminated with the THz waves, excited carriers are created in the devices, resulting in the generation of electric signals. For example, doped Ge crystals are known to exhibit THz photoconductivity through the generation of excess carriers in impurity levels whose energy corresponds to the THz photon energy [4,5].

It also has been demonstrated that nanoscale islands connected to electrodes, such as superconductor junctions [6], CNT quantum dots (QDs) [7] and InAs QDs [8] work as THz detectors. In these devices, the THz-detected signal is produced via electron tunnelling driven by the THz photon energy (THz photon-assisted tunnelling; Figure 3).

The photon-assisted tunnelling is based on a theory of the interaction of a nanoscale island with an electromagnetic wave, which was proposed by Tien and Gordon in 1963 [9]. The essence of their discussion is that new energy bands, the so-called photon sidebands, are formed by the a.c. electric potential of the electromagnetic wave at intervals of nhf (n: integer number, h: Plank constant, f: frequency of the electromagnetic wave) [9,10].

Figure 4 shows the experimental results of the THz photon-assisted tunnelling in the CNT-QD [7]. As schematically shown in Figure 4(a), the CNT-QD structure has source and drain electrodes with a separation of ~600 nm and a side-gate electrode, all of which were patterned with electron-beam lithography. In this device, electrons are confined to a very small area of 1×600 nm^2, forming the QD.

Differently from the black curve for the data without the THz irradiation, new satellite current peaks are generated for the THz-wave illumination. It is also seen that its position relative to gate voltage shifts in the positive direction with increasing frequency, f, of the THz wave. The inset of Figure 4(b) shows that the energy spacing, $\kappa \Delta V_G$, between
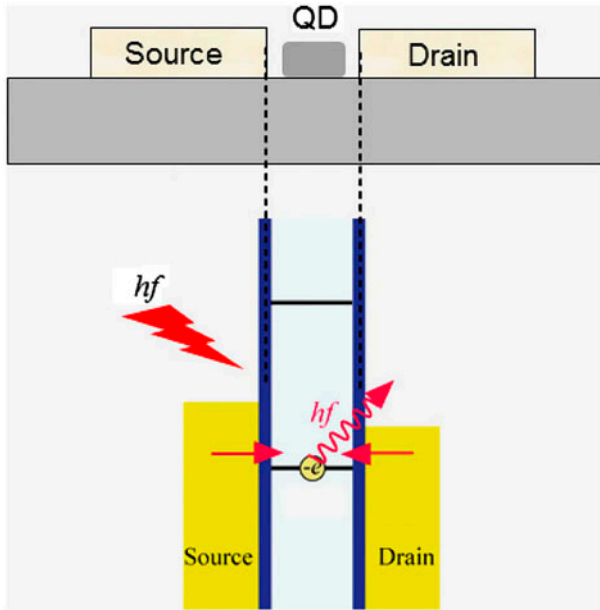
Figure 3. Schematic diagram of the photon-assisted tunnelling in a quantum dot. When electrons in the quantum dot interact with photons, a new current flows via inelastic tunnelling, i.e. photon-assisted tunnelling.

the original peak and the satellite peaks is proportional to the photon energy, hf, of the THz wave. This feature agrees with the generation of the photon sidebands [9,10], indicating the evidence of the photon-assisted tunnelling. Because the position of the photon sidebands relative to the gate voltage is proportional to f, by sweeping the gate voltage, the CNT-QD works as a frequency-tunable THz detector.

2.2.   *Single THz photon detector*

Ultimate sensitivity of the electromagnetic wave detection is that the detector is able to sense individual photons. For such single-photon detection, the optical region is advantageous because the photon energy is higher due to its higher frequency. In fact, for near-IR, visible, and ultra-violet regions, there are well-established single-photon detectors such as photomultiplier tubes, semiconductor avalanche photodiodes, and superconducting transition edge sensors. In the THz region, on the other hand, the development of the single-photon detector is a formidable task, because the photon energy of the THz wave, 1–100 meV, is much smaller than that in the optical frequency regions. In the photomultiplier tubes, even an incident single optical photon induces the carrier cascading process in the tubes, resulting in the generation of observable signals. However, such an electronic process is difficult to induce with the much smaller photo energy of the THz wave.

Nevertheless, the application of nanostructured electronic devices is substantially improving this situation. At present, there are three types of single THz photon
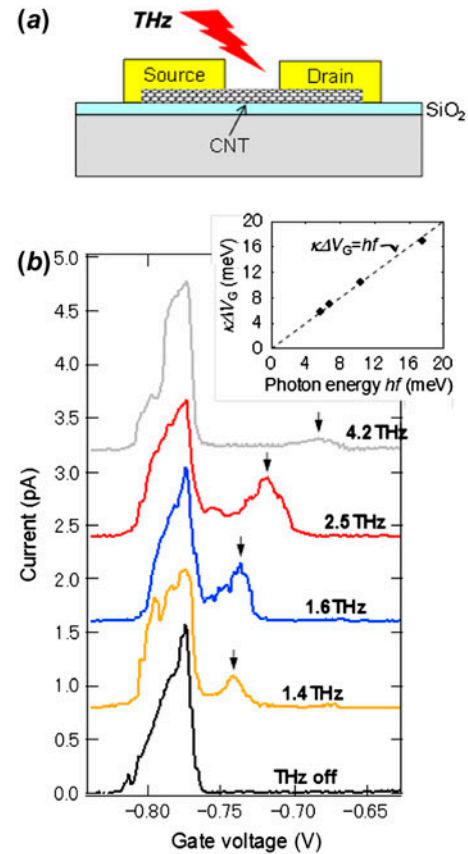

Figure 4. (*a*) Sketch of a carbon nanotube quantum dot. (*b*) Source–drain current I_{SD} versus gate voltage V_G for the frequency of the THz irradiation, f = 1.4, 1.6, 2.4, and 4.2 THz. The experimental curves for the THz irradiation are offset by multiples of 0.8 pA for clarity. The inset shows the energy spacing, $\kappa \Delta V_G$, between the original peaks and the satellite peaks as a function of the photon energy, hf, of the THz wave. The dashed line in the inset is an eye guide corresponding to $\kappa \Delta V_G = hf$. Reprinted with permission from [7].

detectors: semiconductor QD [11], superconducting nano-bolometer [12,13], and CNT transistor [14]. As an index characterising the detection sensitivity, a noise-equivalent power (NEP) is often used. The NEP simply characterises the weakness of the detectable radiation and hence a lower NEP is equivalent to higher sensitivity. In the semiconductor QD detector, electron tunnelling through the QD is modulated with the creation and recombination of THz-excited carriers in the QD and consequently the tunnel current is largely changed even via the event of the single THz photon absorption. The NEP value of the QD detector reaches 10^{-22} W Hz$^{-1/2}$ at 50 mK [11]. The superconducting nano-bolometer utilises a temperature rise via THz absorption, in which the use of the nanoscale sensing area (100–600 nm) enables the occurrence of a sufficient signal for the single THz-photon absorption. In [12] and [13] it was reported that the NEP value is estimated to be 10^{-20} W Hz$^{-1/2}$ at 65 mK.

The operation of the semiconductor and superconductor single THz photon detectors needs a very low temperature
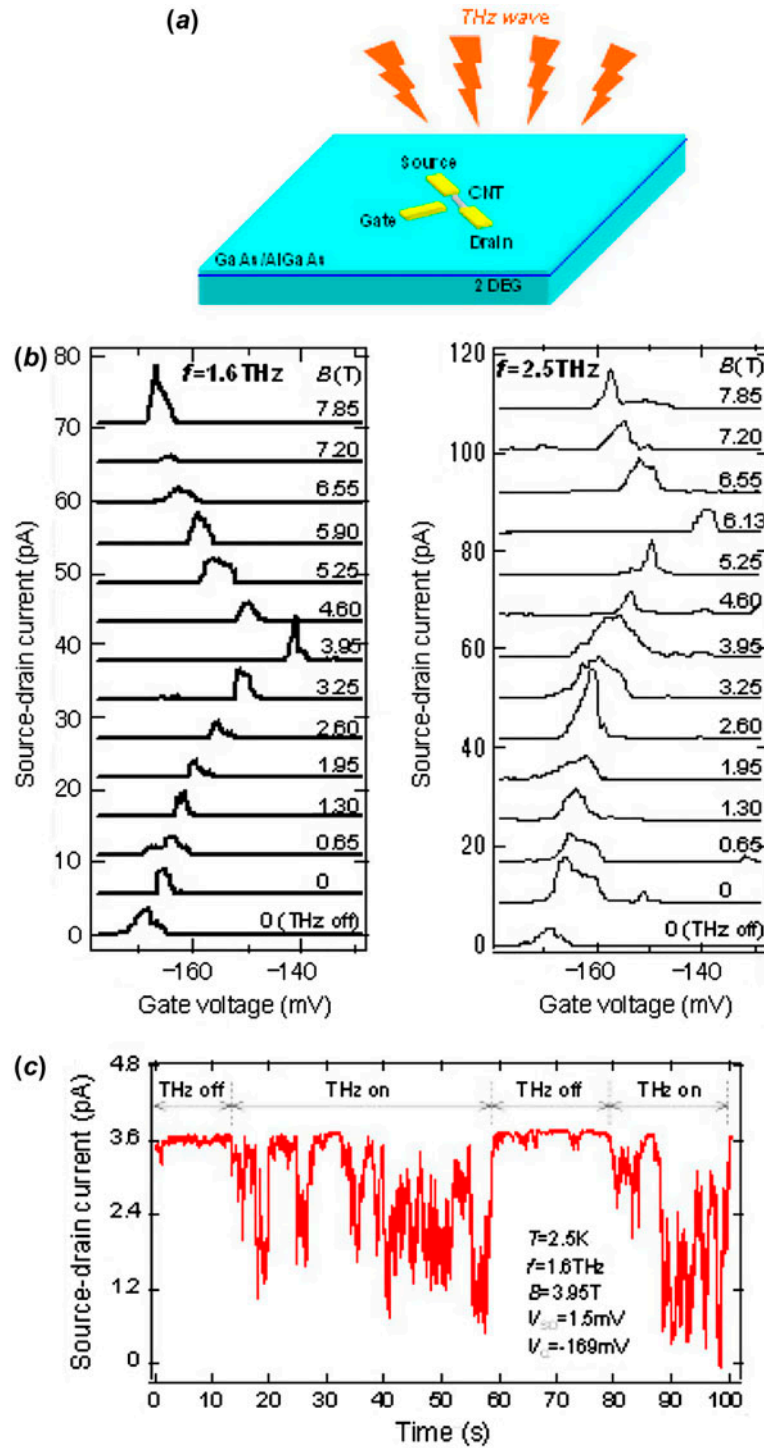
Figure 5. (*a*) THz-photon detector with the CNT/2DEG hybrid device. (*b*) Magnetic field dependence of source–drain current versus gate voltage of the CNT under the THz irradiation. The magnetic field *B* was applied to the detector perpendicular to the 2DEG plane, and the *B* values in units of Tesla (T) are given on the right-hand side of the figures. The data with the THz irradiation are offset for clarity. (*c*) Temporal trace of the THz-detected signal (the CNT-SET current) as the THz irradiation is cycled on and off. In this measurement, THz cyclotron emission radiated from another 2DEG was used with a very low intensity of ∼0.1 fW. Reprinted with permission from [14].
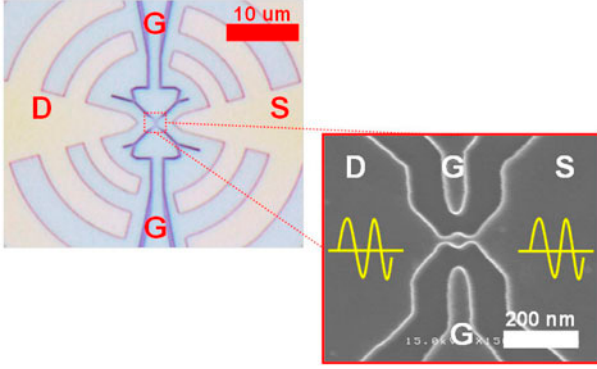
Figure 6. Optical microscope picture of a Si-QD integrated with a log-periodic antenna. Right: scanning electron microscope picture of the Si-QD patterned at the centre of the antenna.
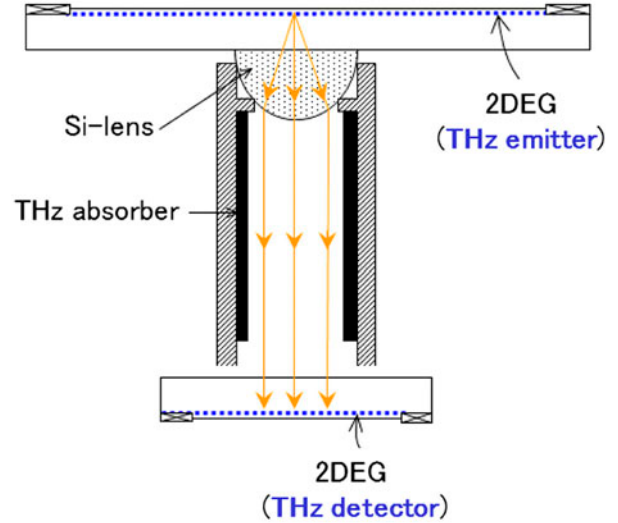

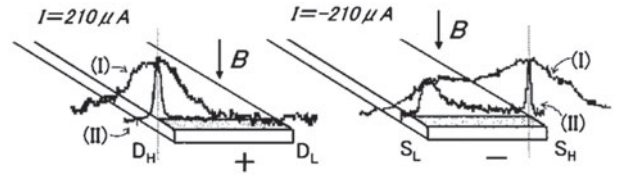Figure 7. Scanning THz microscope based on a solid immersion lens.

Figure 8. Intensity profiles of the THz cyclotron emission along junction regions of the drain contact (+) and the source contact (−) at the source–drain current of 210 μA. The data are taken with (I) the remote Si lens and (II) the Si solid immersion lens (as shown in Figure 7). For clarity, the peak intensities of the signal are normalised. Reprinted with permission from [25].

(<0.3 K). This is because the photon energy of the THz wave is similar to the thermal energy, ~ 26 meV, at room temperature. The environment below 0.3 K forces one to use a dilution refrigerator or a ^{3}He refrigerator, restricting the range of practical uses.

An alternative device for the single THz photon detection is the CNT-based transistor [14]. The CNT is expected to be used as a building block for future nano-electronics, nano-photonics and nano-mechanics owing to its unique one-dimensional structure [15]. IR sensors [16,17] and THz bolometric detectors [18] based on the CNT transistors have been successfully developed. In the following, I explain in detail how the use of the CNT transistor leads to the realisation of the single THz photon detection.

In conventional detectors, one-photon absorption generates only one electron even if a quantum efficiency of 100% is achieved. This restricts the detection sensitivity. In order to tackle this problem, a newly designed device has been created: the CNT transistor is integrated with a GaAs/AlGaAs heterostructure chip containing a two-dimensional electron gas (2DEG) (Figure 5(*a*)). The integrated structure has two separate roles: THz absorption by the 2DEG and signal readout by the CNT. In the CNT transistor, source and drain electrodes are located at a very close distance of ~ 600 nm. Such a nano-scale channel makes the device a single-electron transistor (SET), in which the source–drain current is induced by one-by-one electron tunnelling through the channel. This feature makes it possible to detect a single electron with the CNT-SET. The mechanism of the single THz photon detection with this device is that the CNT-SET senses electrical polarisation induced by THz-excited electron–hole pairs in the 2DEG. Since the SET works as a single-electron sensor, the CNT-SET is expected to detect a single THz-excited carrier, i.e. single THz photons.

Figure 5(*b*) displays the THz response of the 2DEG/CNT device at 2.5 K and the dependence on magnetic field, *B*, applied perpendicular to the 2DEG plane. As seen in the transport properties of the CNT without the THz irradiation,

the oscillatory behaviour of the source–drain current is characteristic of the SET operation. The results of Figure 5(*b*) show that the THz irradiation causes a shift in the current peak position in the direction of positive gate voltage. The data for the irradiation at 1.6 THz reveals that the shift is monotonically enhanced with increasing *B* up to 3.95 T, then decreases when *B* is further raised beyond $B = 3.95$ T. On the other hand, in the case of the 2.5 THz irradiation, the *B* value for the maximum of the peak shift changes to 6.13 T.

The physical meaning behind the features seen in Figure 5(*b*) is as follows: in the presence of perpendicular magnetic field, the energy state of the 2DEG forms Landau levels (LLs) due to the quantisation of electron cyclotron motion. When the photon energy, hf, of the THz wave is equal to LL separation eB/m^*, of the 2DEG, the 2DEG absorbs well the THz wave (cyclotron resonance). Here, *e* is the elementary charge and m^* is the cyclotron effective mass for the crystal used. The experimental data ($B = 3.95$ T for $f = 1.6$ THz and $B = 6.13$T for $f = 2.5$ THz) reveal that the f value is proportional to the B value for the maximum of the peak shift, which is consistent with the characteristic

of the cyclotron resonance. Furthermore, from these data, the associated m^* value is derived to be $0.067m_0$, where m_0 is the free electron mass. This value agrees well with the cyclotron effective mass for a GaAs-based 2DEG [19]. These facts indicate that the current peak shift of the CNT-SET is caused by the THz resonant absorption of the 2DEG.

Figure 5(c) displays the temporal behaviour of the THz signal (the CNT-SET current change associated with the current peak shift) for an on/off sequence of the THz irradiation at $B = 3.95$ T and $f = 1.6$ THz. The intensity of the THz source used here is as low as the order of 0.1 fW. This result shows that the CNT-SET current was stable for the THz off, whereas it repeatedly switched during the THz irradiation. This behaviour means that the CNT-SET detects temporal processes of excitation and recombination of THz-excited carriers in the 2DEG, demonstrating the detection of a small number of THz photons. The NEP of this THz-photon detector is estimated to be 10^{-18}–10^{-19} W Hz$^{-1/2}$ at 2.5 K.

The CNT THz detector can work at 6–7 K. This performance eliminates the use of a dilution or ^{3}He refrigerator with low cooling capacity and complex systems. The device, therefore, can be used in a standard ^{4}He refrigerator or a compact cryo-free mechanical refrigerator with much higher cooling capacity and much greater ease of use.

In order to make single THz photon detectors more powerful and user-friendly, two important issues have to be resolved. First is the development of high-performance refrigerators. As the performance of cryo-free, mechanical systems such as Gifford–McMahon and pulse-tube refrigerators is rapidly improving, compact, low-vibration and automatic-controlled cooling systems are emerging. By incorporating such a system, single THz photon detectors will find a broader range of applications.

The second crucial issue is low quantum efficiency, namely low coupling efficiency with the THz wave. This problem originates from the fact that the sensing area of all the single THz photon detectors is of nanometre scale (100–600 nm), which is much smaller than the wavelength of the incident THz wave. One effective approach for enhancing the quantum efficiency is to implement appropriate antennas into the detectors. Integrating the superconducting nanobolometer with the coplanar waveguide structure of the planar antenna has been already attempted [13]. For the improvement in the QD-based detector, Crespi et al. [20] reported a unique structure: a Si-QD sensor integrated with a log-periodic antenna (Figure 6). Their simulation demonstrated that the THz field is concentrated on the edge region of the antenna to which the QD is connected. This result theoretically indicates the improvement in the quantum efficiency. Another promising method is to combine the THz detectors with plasmonic structures. Miyamaru et al. [21] reported that when a metal–hole array is illuminated with the THz wave, the THz electric field is concentrated in the edge region of the metal hole. By integrating such an arrayed metal–hole structure with the single photon detectors, an efficiency enhancement is expected. Seo et al. showed that the THz electric field is dramatically enhanced in a metal nanogap by a factor of 10^3 [22], whose use would be a possible solution.

Recent progress in microwave technology has enabled photon correlation measurements even for the microwave region where photon energy is much lower than that of THz photons. Bozyigit and co-workers [23,24] reported antibunching of microwave photons in a superconducting electronic circuit and state tomography.

3. THz imaging

As mentioned in the introduction, the visualisation of objects with THz waves is one of the central technologies in the THz research field. The THz imaging potentially enables nondestructive safety inspection, medical checks, astro-imaging, and analysis of various materials and bio-molecules.

In spite of the wide availability, many researchers have suffered from a big issue – low spatial resolution of the THz imaging. Generally, the spatial resolution of the electromagnetic wave imaging is inherently limited by its wavelength owing to the wave diffraction. The disadvantage of the THz wave is that its wavelength is much smaller than that of the IR, visible, and ultra-violet light. This issue is particularly critical for examining micro- and nano-scale objects such as nano-materials, cells, and molecules.

As a result of much effort by THz researchers, however, several useful and powerful technologies of high-resolution THz imaging have been produced. In this section I explain three types of advanced imaging techniques: solid immersion lens, camera imaging, and near-field imaging.

3.1. Solid immersion THz lens

In a standard optical imaging system like the use of a lens, spatial resolution of optical images is proportional to the wavelength of the light. The solid immersion lens exploits the fact that the wavelength in a material with high dielectric constant is reduced compared to that in vacuum. Therefore, the use of a lens with a large refractive index results in obtaining high imaging resolution.

Figure 7 depicts an example of the THz imaging system based on the solid immersion lens [25]. A hyperhemispherical lens made of Si is in contact with the back surface of a sample. The sample is a 2DEG in a GaAs/AlGaAs heterostructure. THz emission from the 2DEG is radiated as a consequence of inter-LL transitions of electrons under a magnetic field, i.e. cyclotron emission [25–27]. The focal point of the lens is designed to be on the 2DEG layer of the sample. The cyclotron emission from the focal point is collimated via the lens and is guided through a metallic light pipe
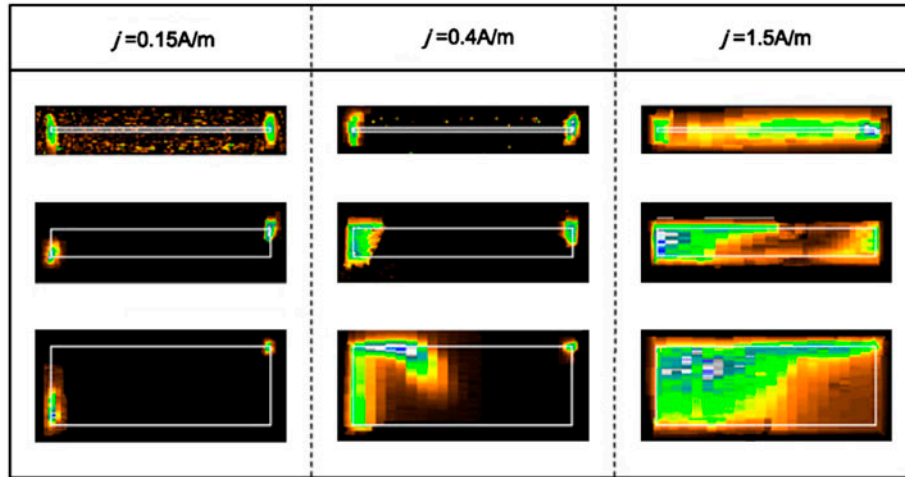
Figure 9. THz emission images at three current densities $j = 0.15$, 0.4, and $1.5\,A\,m^{-1}$ and for the three samples with different channel widths $W = 20$, 300, and $1200\,\mu m$. The white solid lines denote the 2DEG-channel boundaries of the samples. Reprinted with permission from [27].
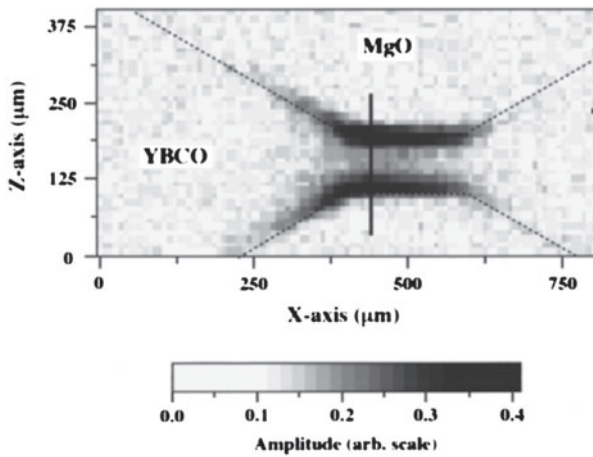

Figure 10. Imaging of the supercurrent distribution in the high-temperature superconductor (YBCO thin films), obtained with THz imaging. Reprinted with permission from [31].

to a THz detector. Off-axis light is cut by a black polyethylene pipe. The sample is scanned relative to the lens with an X–Y translation stage, while the optical system including the detector is stationary. The relatively large refractive index of GaAs and Si ($n \sim 3.4$) leads to imaging resolution higher than that obtained with a remote lens system.

Figure 8 compares the resolution between the remote lens and the solid immersion lens. It is clear that the solid immersion lens system provides well-resolved emission profiles. The resolution of the solid immersion lens system is about $50\,\mu m$ at $130\,\mu m$, the wavelength of cyclotron emission in vacuum. This value is improved by a factor of 6, compared to the resolution ($300\,\mu m$) for the remote Si lens.

Using this THz microscope, the THz emission distribution was imaged for the 2DEG samples with different channel widths of $W = 1.2$, 0.3, and $0.02\,mm$ with the channel length $L = 4\,mm$ (Figure 9) [27]. All the samples were fabricated from the same GaAs/AlGaAs heterostructure crystal. In the widest sample ($W = 1.2\,mm$), the emission takes place mostly in the two diagonally opposite corners and in a localised region near the source contact. In the data for $W = 0.3\,mm$, the emission expands more into the interior 2DEG region. Furthermore, when $W = 0.02\,mm$, the emission takes place over the entire region of the interior 2DEG channel.

The underlying origin of this phenomenon is as follows: in the 2DEG devices under magnetic field, it is known that high electric field is concentrated in the two diagonally opposite corners, which are also electron entry and exit corners [28]. It follows that as the current increases, electron excitation into higher LL starts in the vicinity of the two current contacts. The observed features of the THz emission images are consistent with such electron dynamics. In addition, earlier works revealed that the scattering length of the excited electrons in the 2DEG reaches a macroscopically long length of $\sim 100\,\mu m$ [29,30]. This means that the electrons travel the macroscopic distance to lead to an appreciable generation of the cyclotron emission. The significant channel-size effect observed can be reasonably understood as arising from the competition between W and the scattering length. (For the details, see [27].)

As demonstrated above, THz imaging succeeds in directly probing the transport of non-equilibrium electrons in semiconductors. It is thus expected that the availability of THz imaging will spread over research on charge transport in other solid-state devices. Besides, superconductors, nano-carbons, polymers, etc. are interesting targets for THz imaging. In fact, Shikii et al. previously reported the visualisation of supercurrent distribution in high-temperature superconductivity by use of THz imaging (Figure 10) [31].
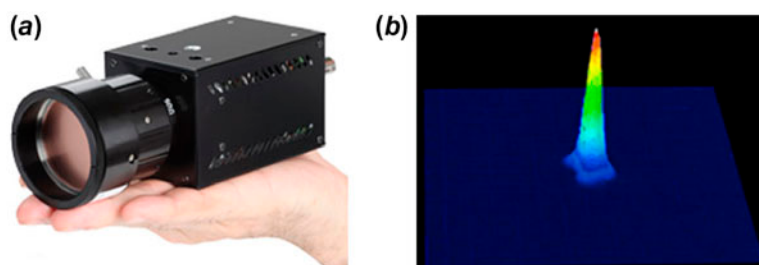
Figure 11. (*a*) Uncooled THz camera. (*b*) Spatial pattern of THz beam radiated from a quantum cascade laser, taken with (*a*). Reproduced courtesy of NEC Corporation.
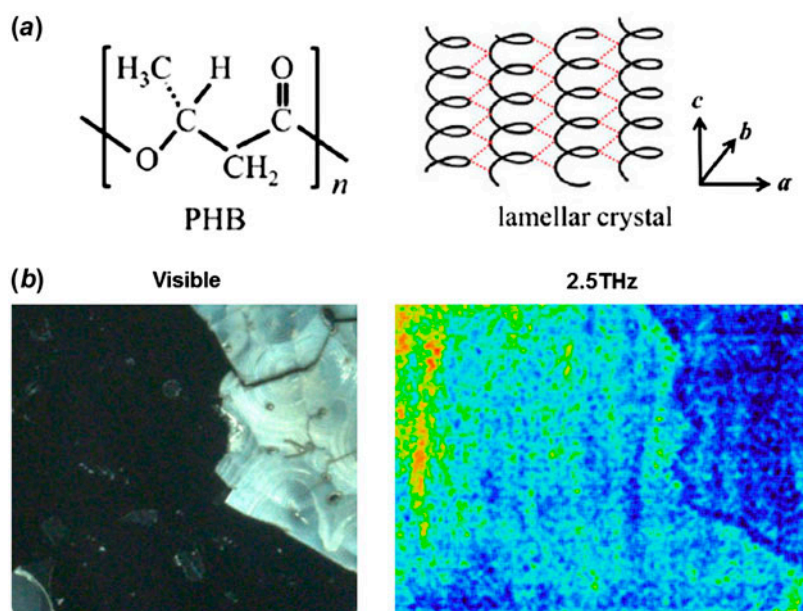

Figure 12. (*a*) Chemical structure of PHB and sketch of molecular structure in lamellar crystal. Reprinted with permission from [35]. (*b*) Visible and THz images of the crystalline PHBs on the Si substrate. The THz image was taken for 2.5 THz irradiation.

3.2. THz camera

The above method is based on a scanning system and hence obtaining one THz image takes a long time, typically the order of minutes to hours. When an object under investigation is moving in space and/or its spatial properties are changing in time, real-time THz imaging or video camera imaging is necessary. For this purpose, two-dimensional arrayed THz sensors have been developed [32–34] and their performance such as sensitivity and bandwidth is steadily improving. Because the THz camera is expected to be in much demand in industry and security fields, in many instances this type of device works at room temperature. For applications to basic science, especially when highly sensitive measurements are needed, cooled THz cameras are often used.

For the development of the THz camera, there are two approaches: an extension to the higher frequency region of the microwave camera and an extension to the lowerfrequency

region of the IR camera. Figure 11(*a*) shows an example of an uncooled THz camera, which is based on arrayed IR bolometers. Its specification is NEP $\sim 10^{-10}$ W Hz$^{-1/2}$ at 4 THz, a frequency range of 1–7 THz, and a pixel number of 320×240 with 23.5 μm pitch [32]. Using this camera, the spatial beam profile of a THz quantum cascade laser is clearly visualised (Figure 11(*b*)).

As a target of the THz camera imaging, the study of spatial properties of biological molecules and polymers is a challenging and intriguing subject because it enables us to obtain direct information on the dynamics of higher-order structures of the molecules. Figure 12 shows the study of spatial properties of polymers with the THz camera imaging. The sample investigated is crystalline polyhydroxybutyrates (PHBs). The PHB is known to have a role of energy storage in cells. Molecular chains of the crystalline PHB make up a lamellar crystal in which helicalstructures are aligned with
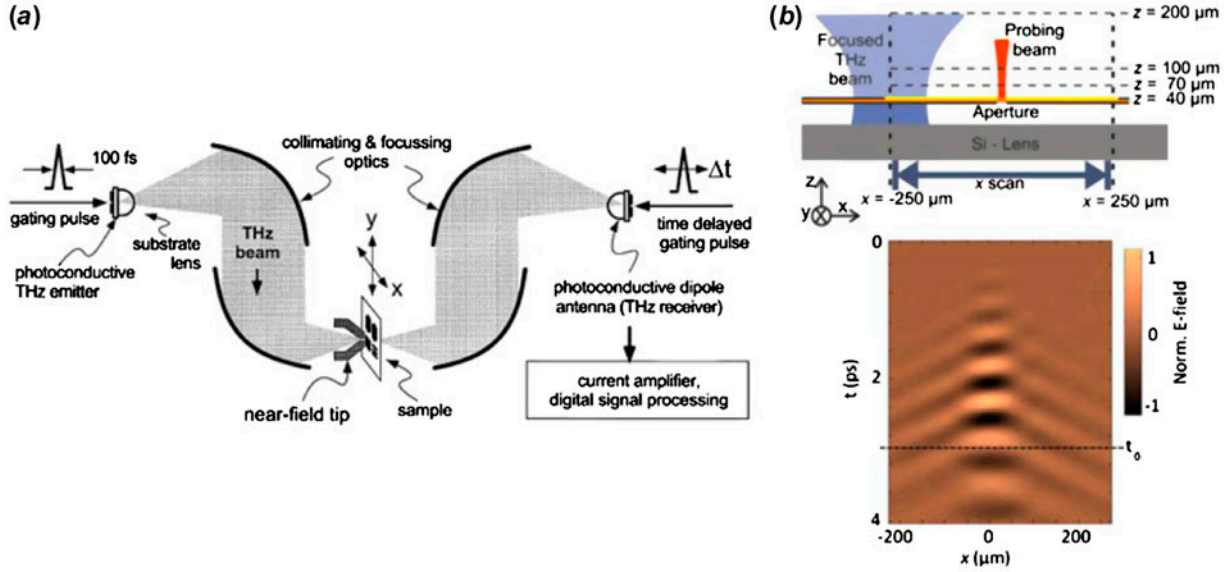
Figure 13. Aperture-based near-field THz imaging; (*a*) reprinted with permission from [46] and (*b*) reprinted with permission from [48]. (*b*) Experimental setup and results for spatial and temporal imaging of surface plasmon polariton waves.
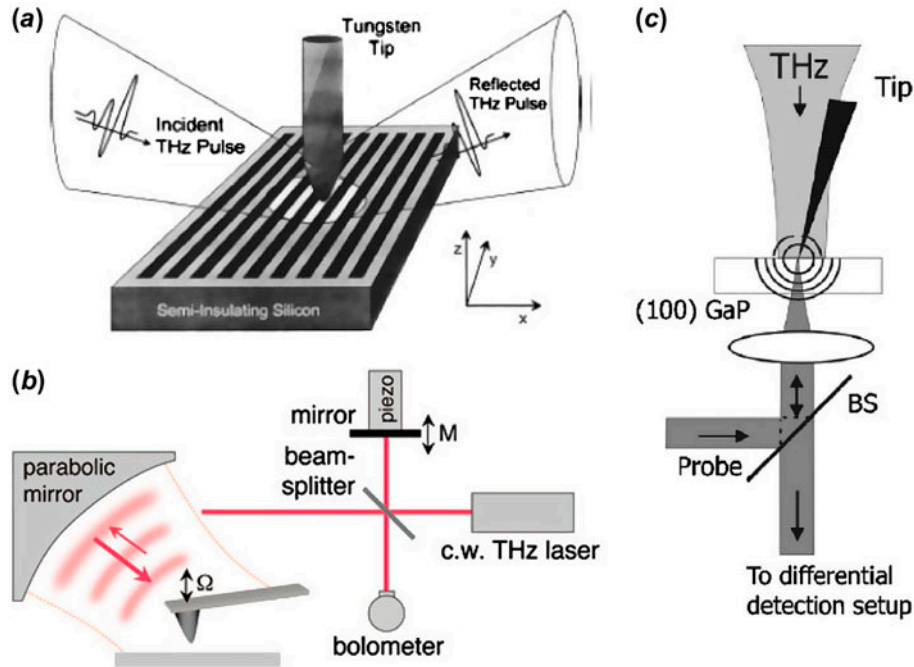

Figure 14. Probe-based near-field THz imaging; (*a*) tungsten tip (reprinted with permission from [50]), (*b*) metal-coated cantilever (reprinted with permission from [51]), and (*c*) sharpened antenna (reprinted with permission from [52]).

regularity (Figure 12(*a*)) [35,36]. The PHBs absorb the THz wave due to their unique helical structures and hydrogen bonding [35,36].

The THz camera imaging was applied to the crystalline PHB sample attached on a Si substrate. A THz laser irradiated the sample and the two-dimensional distribution of the transmitted THz waves was mapped out by the THz camera

at room temperature. Figure 12(*b*) shows the optical and 2.5 THz image of the crystalline PHBs on the Si substrate. A boundary between the PHBs and Si is clearly seen, indicating the THz absorption by the crystalline PHBs. The frequency dependence of the THz image was also observed, which was consistent with the absorption spectra of the crystalline PHBs [35,36].
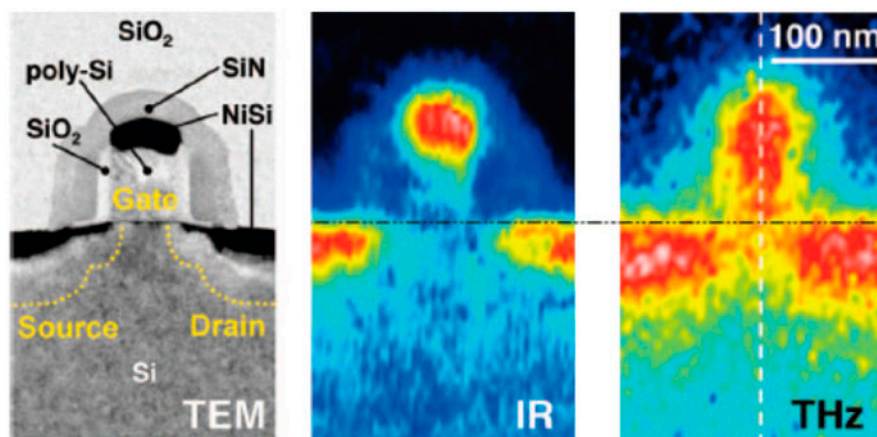
Figure 15. Left: transmission electron microscope image of a single semiconductor transistor. Middle: IR image of the transistor in left. The wavelength used here is about $11\,\mu$m. Right: THz image of the transistor in left. The wavelength used here is about $118\,\mu$m. The spatial resolution is the same between IR and THz images. Reprinted with permission from [51].
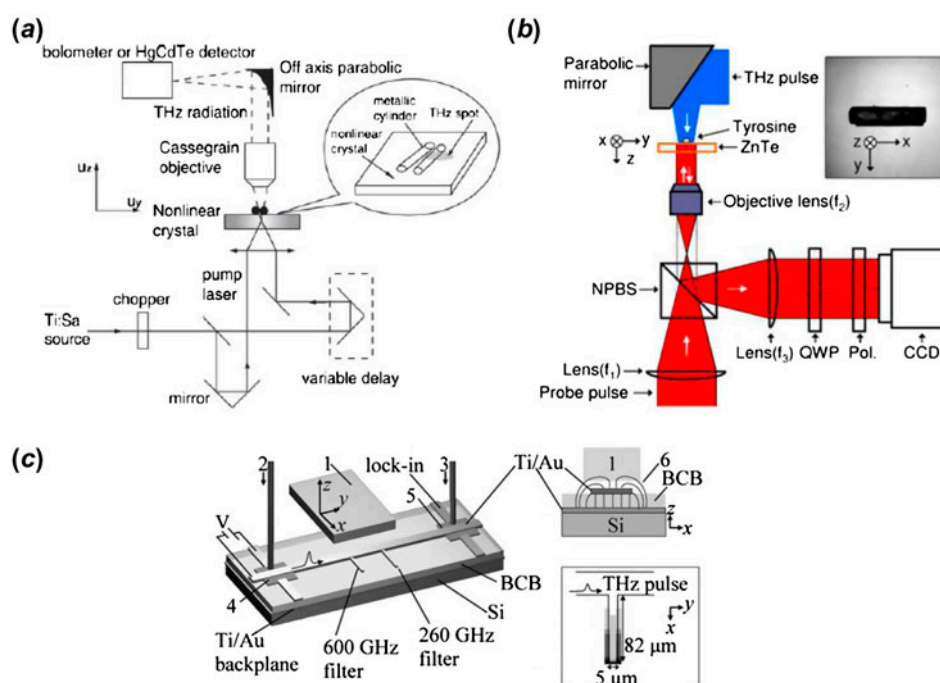

Figure 16. Near-field THz imaging with sub-wavelength THz sources; (*a*) reprinted with permission from [54], (*b*) reprinted with permission from [55], and (*c*) reprinted with permission from [56].

This experiment is a first step toward THz bio-imaging and ultimately single-molecule THz imaging. The THz analysis of individual molecules is a future challenge.

3.3. *Near-field THz imaging*

Though the solid immersion lens system leads to relatively high resolution and the THz camera provides real-time images, the resolution of these methods is still determined by the diffraction limit. A powerful technique for overcoming the diffraction limit and for obtaining a sub-wavelength

resolution is to use near-field imaging [37,38]. When an electromagnetic wave is shone onto an object smaller than the wavelength, a localised evanescent field (near-field) is generated just at the surface of the object. The size of the evanescent field is determined primarily by the object size and not the wavelength. By illuminating with and/or detecting the evanescent field, it is possible to get resolution beyond the diffraction limit.

Historically, the first idea of the near-field imaging was presented by E.H. Synge in 1928 [39]. He proposed that a 10-nm aperture much smaller than the light wavelength
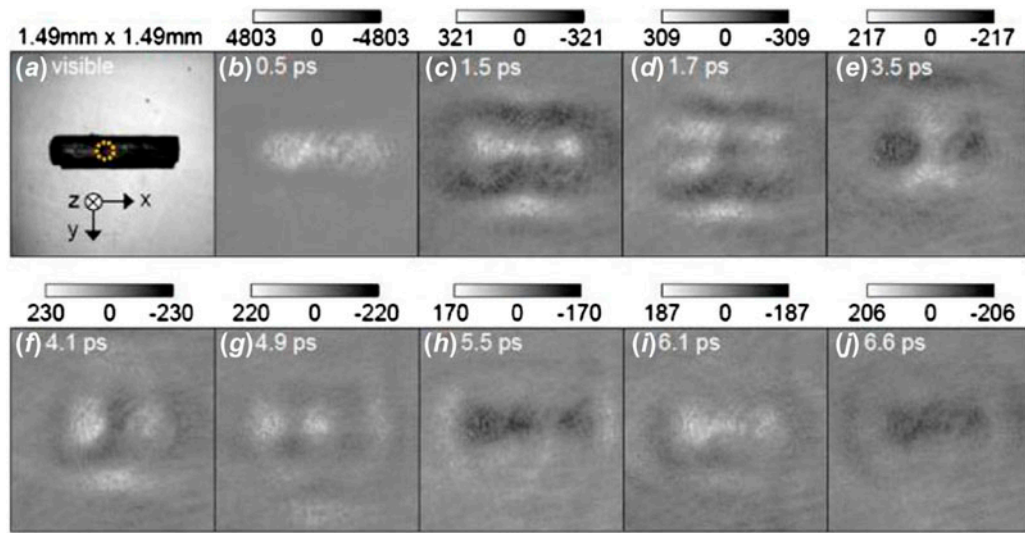
Figure 17. (*a*) Optical photograph of the grain of tyrosine sample on a (110) ZnTe crystal. Dotted circle denotes the location where the temporal profiles of the THz electric field distribution were extracted. (*b*)–(*j*) Spatial and temporal mapping of the THz electric field in the sample of (*a*). Scale bars show the relative strength of the THz electric fields. Reprinted with permission from [55].

is scanned closely over a sample surface. Inspired by his idea, near-field imaging was experimentally realised in the microwave region in 1972 [40] and then in the visible light region in 1984 [41].

Generally, near-field imaging systems are of an aperture type or an aperture-less (scattering) type. In the visible and near-IR regions, either a tapered, metal-coated optical fiber (aperture type) [42] or a metal tip (aperture-less type) [43] is used. In the microwave region, either a sharpened waveguide (aperture type) [44] or a coaxial cable (aperture-less type) [45] is used. Since the intensity of the evanescent field is very weak, the realisation of near-field imaging requires highly sensitive detection schemes, such as a high transmission wave line and a highly sensitive detector.

It was not until after 1998 that the near-field technique was applied to the THz region. Since the first demonstration by Hunsche et al. who used a metal cone (aperture type) [46], several other techniques have been proposed and attempted. At the moment, the near-field imaging in the THz region is generally classified into three types and their features are summarised below. Passive near-field THz imaging without external THz sources is also presented.

3.3.1. Aperture

The first demonstration of the near-field THz imaging was made using a metal cone with a sub-wavelength aperture (Figure 13(*a*)) and the resolution obtained was better than $\lambda/4$ (55 μm) [46]. This method, however, has the drawback of low wave transmission through the small aperture, which requires the detection of very weak waves. Mitrofanov et al. fabricated a GaAs pyramid-like structure protruding through the aperture and enhanced coupling
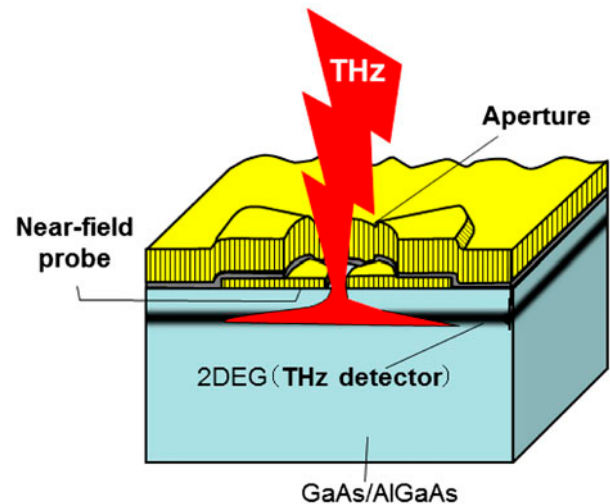
Figure 18. Schematic view of the integrated near-field THz sensor for active and passive imaging.

between the incident THz waves and the aperture, with the resulting resolution of 7 μm [47]. Combining the near-field THz imaging with the THz-TDS, Mueckstein and Mitrofanov achieved imaging of surface plasmon polariton waves, which was formed near a tightly focused THz beam on a metallic surface (Figure 13(*b*)) [48]. In this measurement, the electric field distribution of the surface plasmon polariton wave was successfully imaged in both space and time domains.

In the GHz region, a high-transmission waveguide made from dielectric materials can be used. The resolution of 20 μm at 80 GHz ($\lambda/200$) using a sharpened waveguide was reported [49]. Creating a low-loss waveline suitable

for near-field THz imaging would enable measurements similar to the fiber-based near-field imaging used in the optical region.

3.3.2. *Metallic probe (aperture-less)*

The metallic probe type (aperture-less technique) provides high spatial resolution because the resolution is chiefly determined by the diameter of the probe tip. It is possible to use conventional probes such as metal-coated cantilevers and metallic tips, as used in the atomic force microscope and the scanning tunnelling microscope. In this type of method, the evanescent field is scattered by the probe tip and in some cases its intensity is enhanced. The evanescent field is then transformed into the propagation field, which is detected by a remote detector. A tungsten tip [50], a metal-coated cantilever [51], and a sharpened antenna [52] (Figures 14(a)–(c)) have been used and resolutions of 150 nm, 40 nm and 18 μm, respectively, were reported.

Although this technique provides a considerably higher resolution than the aperture type, it sometimes has the problem of separation from the far-field component of an incident wave, which generates a large background signal. For this reason, in most instances the probe position is modulated and the synchronously detected signal is measured. This approach makes the entire system and its operation complicated and the fluctuations of the background signal often prevent accurate measurements. In order to resolve these problems, Huber et al. reported that the background signal can be reduced by measuring a high-order signal of the synchronously detected signal [51].

As a notable example of the probe-based, high-resolution THz imaging, Figure 15 displays the visualisation of spatial distribution of carrier concentrations in a nano-scale semiconductor transistor [51]. They used a metal-coated cantilever that was illuminated by the THz gas laser (see Figure 14(b)). As a result of the interaction between the near-field THz waves and the electrons in the transistor, the near-field THz waves were transformed into the propagation field, which was detected by a bolometer. As seen in the experimental results of Figure 15, the THz image shows a much higher contrast map of the carrier concentration compared to the IR image, although the two images have the same resolution. In general, studying the interaction between materials and light provides rich information about physical and/or chemical properties corresponding to the wavelength. For example, it is possible to examine electronic transitions in molecules in the visible light and ultraviolet regions and molecular vibrations and rotations in the near- and mid-IR regions. The THz map here successfully demonstrates that THz imaging is useful for visualising typical electron concentrations in semiconductor nanoscale devices. The authors of [49] mentioned that their measurement probes as few as about 100 electrons.

3.3.3. *Sub-wavelength THz source*

An alternative method is to use a THz emission spot whose size is smaller than the wavelength (Figures 16(a)–(c)). It is known that when an optical beam is shone onto a nonlinear optical crystal like ZnTe, it generates THz emission. If the incident optical beam is tightly focused, the radiation region of the THz emission in the close vicinity of the crystal surface (in the near-field region) is reduced to the sub-wavelength size. This indicates that the surface of the nonlinear optical crystal works as a sub-wavelength THz source. This method has the following advantageous features: (i) the properties of the incident THz beam are determined solely by the optical beam and the nonlinear optical crystal and not by sample topography; (ii) this is a more simplified method compared to the probe type because the sample is placed directly on the crystal surface and the focused optical beam is scanned relative to the crystal surface. However, it should be noted that since such a nonlinear optical crystal emits broadband THz radiation, THz imaging for one fixed wavelength is impossible.

References [53] and [54] reported near-field THz imaging based on this method, and the resolution of 20 and 75 μm, respectively, were achieved. Figure 16(a) shows the measurement setup as reported in [54]. By combining this method with CCD detection, Doi et al. demonstrated realtime near-field THz imaging of free induction decay from a tyrosine crystal with the resolution of 70 μm (Figure 16(b)) [55]. Figure 17(a) displays the optical image of the grain of the tyrosine sample on a ZnTe crystal. The dotted circle of Figure 17(a) shows the location where the time profiles of the THz electric field were extracted. Figures 17(b)–(j) show the temporal evolution of the THz electric field distribution measured with increasing delay times. It is seen that the electric field oscillates, suggesting that the cavity modes of the tyrosine crystal, which are determined by its refractive index and its shape, are resonantly excited with the THz pulse.

Another method of this type is to use the evanescent field that is localised on the surface of a THz waveguide made from dielectric materials. It is generally known that the THz waves propagate well in dielectric materials such as a Si rod and that the evanescent field is generated in the near-field region close to the outside surface of such a waveguide. By illuminating the sample with the THz evanescent field and scanning the sample across the waveguide surface, it is possible to perform near-field THz imaging. Cunningham et al. fabricated a guided-wave THz microstrip circuit and demonstrated near-field THz imaging with the resolution of 20 μm (Figure 16(c)) [56].

3.3.4. *Passive near-field THz imaging*

All the techniques introduced above are 'active' imaging, which means that a sample is illuminated with an external THz source and that a reflected or transmitted THz
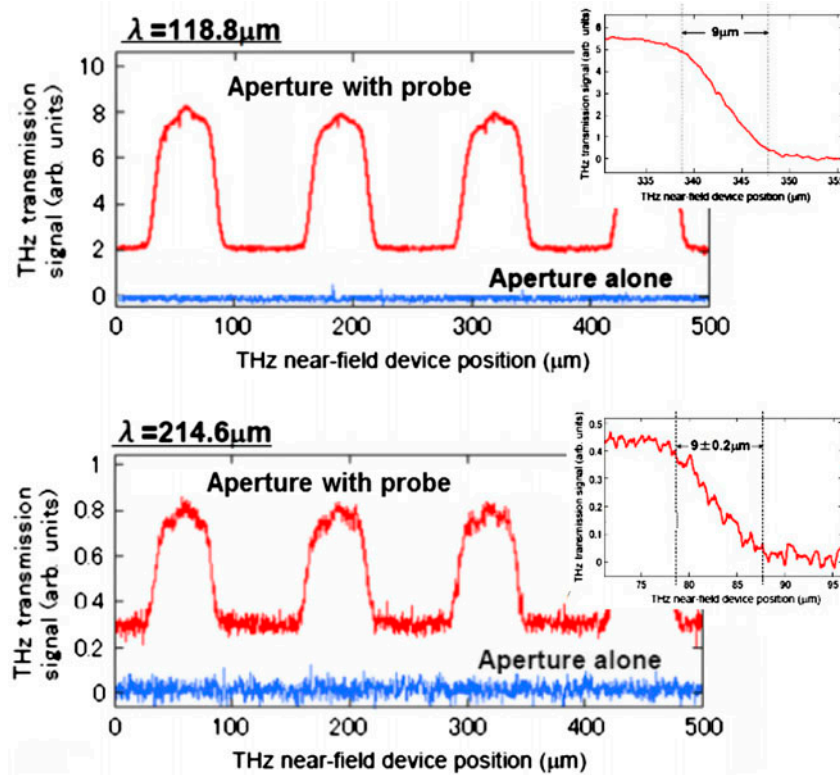
Figure 19. THz transmission signal versus the position of the near-field THz sensors (Figure 18) without and with the probe. The insets show decay curves of the signals in THz transmission distribution.

wave is detected. Although the active imaging provides high-contrast THz images thanks to the use of the THz source, there are some instances where THz emission radiated with energy dissipation of a sample itself needs to be studied, for example, THz emission associated with non-equilibrium electron transport of solid-state devices and THz emission arising from chemical reaction of bio-molecules. For such an investigation, an external THz source is not used and the sample provided under intrinsic energy flow like heat and current is to be measured, which is called 'passive' imaging.

It is easily imagined that the passive near-field THz imaging is a non-trivial task where a very weak THz near-field must be detected without any help of the external THz source. In the mid-IR region, already passive near-field imaging of thermal radiation in metals has been achieved [57,58]. In the THz region, however, there is a difficulty in making similar measurements because the intensity of the thermal (black-body) radiation is peaked at the mid-IR region while it is substantially reduced in the THz region.

Below I introduce a unique method for highly sensitive THz near-field detection: on-chip THz imaging with an integrated semiconductor device. This technique is available for both active and passive imaging [59–61]. The problems of other techniques were low efficiency of near-field detection and complicated systems. The new integrated device enables the near-field THz imaging in a much simpler manner.
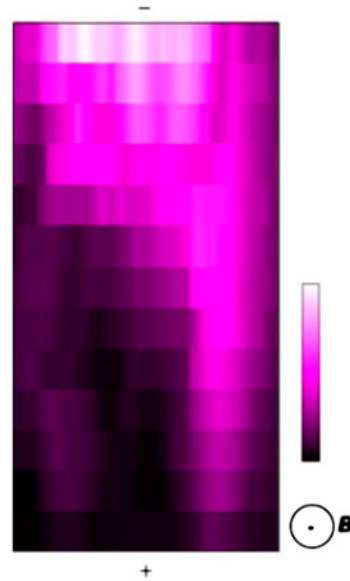
Figure 20. Passive near-field image of THz emission distribution in the 2DEG sample at the current of $160\,\mu$A. The length and width of the 2DEG channel are 400 and $200\,\mu$m. This THz image was taken using the sensor of Figure 18. Here no external THz source was used. Reprinted with permission from [61].

As shown in Figure 18, a sub-wavelength aperture and a planar probe are deposited on a surface of a GaAs/AlGaAs heterostructure chip. The aperture and the probe are insulated by a 50 nm thick SiO_2 layer. The 2DEG, located 60 nm

below the chip surface, works as a THz detector [62]. In this device structure, all components: an aperture, a probe, and a detector are integrated on one GaAs/AlGaAs chip. This scheme eliminates any optical and mechanical alignments between each component, leading to an easy-to-use and robust system.

This device structure has the advantage that the presence of the planar probe changes the distribution of the evanescent field, enhancing the coupling of the evanescent field to the 2DEG detector. This leads to an increase in the detection sensitivity. Moreover, the 2DEG detector is not affected by the far-field wave (background signal) owing to the close vicinity to the aperture and the probe, allowing the detection of the evanescent field alone.

Figure 19 shows the results of the active THz near-field imaging in which THz transmission distribution was imaged by scanning the above device across a sample under the THz irradiation. The sample is made up of a THz transparent substrate, the surface of which is covered at regular intervals by THz opaque Au films. The widths of THz opaque and transparent regions across the scan direction are 80 and $50\,\mu\text{m}$, respectively. Two types of near-field THz devices were used; the aperture plus the probe and the aperture alone. As seen in Figure 19, in the former case, a clear profile corresponding to the THz opaque and transparent regions is visible, whereas in the latter case, there are no observable signals. This feature does not depend on the wavelength of the incident THz wave. These results clearly demonstrate that the distribution of the THz evanescent field is largely enhanced due to the presence of the probe, leading to the improvement in the detection sensitivity.

From the decay curves shown in the insets of Figure 19, the spatial resolution of the near-field THz device (aperture $\sim 8\,\mu\text{m}$) is found to be $9\,\mu\text{m}$, which is beyond the diffraction limit $\lambda/2$ ($107.3\,\mu\text{m}$) for the wavelength of $\lambda = 214.6\,\mu\text{m}$. The present device hence properly functions as a near-field THz imaging detector. The resolution can be improved with reducing the aperture and recently the resolution of 400 nm ($\sim \lambda/540$) has been achieved.

Using this device, passive near-field THz imaging was also demonstrated. Figure 20 displays a passive near-field image of THz emission distribution in another 2DEG sample, which was taken with the same detector as used in the active imaging. Here no external THz source was used. The THz emission from the 2DEG is radiated as a consequence of inter-LL transitions of electrons when the magnetic field and current are applied to the 2DEG. This means that this passive imaging probes the spatial properties of excited electrons in the 2DEG. Interestingly, the THz image reveals the strongly asymmetric distribution between the electron-entry and electron-exit sides. This can be understood in terms of the long scattering length of the excited electrons in the 2DEG [27].

This passive near-field THz imaging technology opens up a new route to examine the inherent natures of various materials such as superconductors, organic conductors, polymers, and molecules.

In general, as the spatial resolution is improved, the intensity of the wave to be detected, especially in the near-field region is strongly reduced because the sensing area becomes small. This situation imposes one to produce a scheme of highly sensitive detection in a tiny region. For future THz nano-imaging, it will be an effective approach to incorporate ultra-sensitive THz detectors as introduced in Section 2.2.

4. THz spectroscopy

The photon energy and the period of the THz wave with 1 THz are about 4 meV and 1 ps, respectively. The physical properties of many important materials lie in this energy and time region, such as the energy gap of a superconductor, the impurity level of a semiconductor, phonon energy, LL separation, and quantised energy separation due to electron confinement in low-dimensional semiconductors. This importance is applicable to other research fields. For example, polymers and bio-molecules have their characteristic frequencies in the THz region and the analysis of THz radiation from celestial objects is expected to elucidate the nature of the solar system and universe. These facts mean that THz spectroscopy will find strong applications in a wide range of fields including physics, chemistry, biology and astronomy. In these fields, THz spectroscopy is expected to give rich information about quantised electron dynamics in solids, chemical bonding, higher-order structures of bio-molecules, dark matters in space, etc.

Representative methods for THz spectroscopy are the Time-Domain Spectroscopy (TDS) and Fourier transform spectroscopy (FTS). In this section, I first explain the main features of TDS and FTS and then introduce frequency-tunable THz emitters and detectors as alternative THz spectrometers. THz spectroscopy is closely linked to IR spectroscopy and the two spectroscopies provide complimentary information. For example, in chemical spectroscopy, IR spectroscopy gives accurate information about the internal structures of molecules such as functional groups, while THz spectroscopy reveals inter-molecular dynamics. However, the THz and IR spectroscopic measurements can not be simultaneously made with one instrument except for a special technique like ultra-broad band TDS [63]. In the latter part of this section, I introduce a novel type of wide-band spectrometer based on graphene, which enables THz and IR spectroscopy with a single solid-state device.

4.1. Time-domain spectroscopy and Fourier transform spectroscopy

THz-TDS is nowadays widely employed in THz research fields [64]. The remarkable feature of this technology is that it allows real-time observation of the oscillatory electric field of the THz wave. This measurement therefore provides
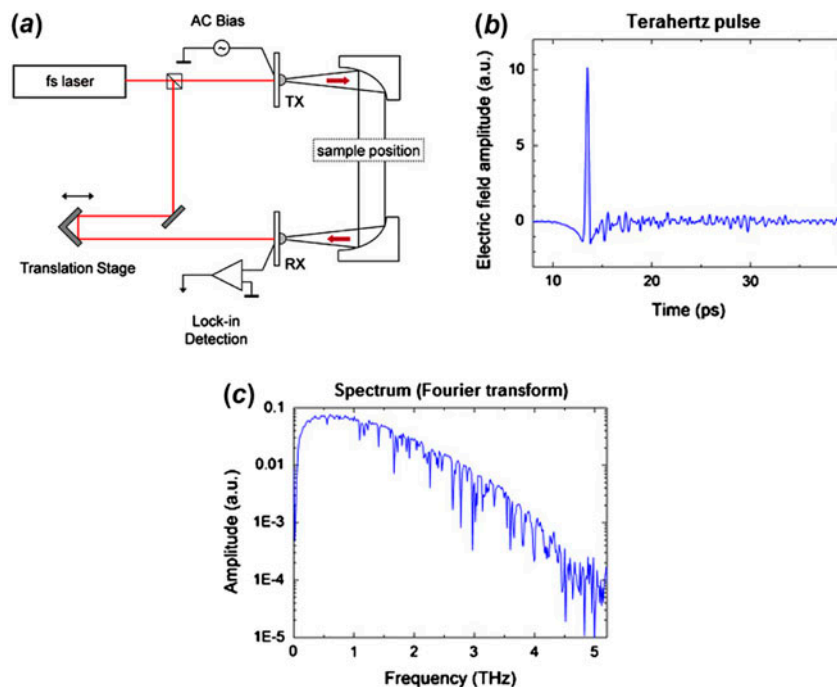
Figure 21. (*a*) Typical setup of the TDS system. (*b*) THz pulse transient in the time domain, taken with (*a*). (*c*) Frequency spectrum of (*b*). Reproduced courtesy of Otsuka Electronics Co., Ltd. and TOPTICA Photonics AG.

direct information on both amplitude and phase of the THz electric field. Furthermore, the THz frequency spectra can be immediately obtained through the Fourier transform of the temporal form of the THz electric field. As emitters and detectors in TDS, a photoconductive antenna and an electro-optic device are usually used. As shown in Figure 21(*a*), when the THz emitter is illuminated with a femto-second pulse laser, the pulsed THz wave is radiated to free space. The THz wave is shone onto a specimen and the transmitted or reflected THz wave is sensed by the detector. The femto-second laser is divided by a beam splitter and also comes to the detector through a movable time-delay stage. The detector responds to the THz wave only when it receives the femto-second laser. By translating the time-delay stage, the time trace of the THz electric field is directly measured. Typical results in the time and frequency domains are shown in Figures 21(*b*) and (*c*). In some instances, the system extends its function to THz spectroscopic imaging by incorporating an $X–Y$ translation stage for moving the specimen. In standard THz-TDS, the signal-to-noise ratio (S/N) shows a maximum in a sub-THz region and substantially decreases above 2 THz as shown in Figure 21(*c*).

The FTS has a long history as a useful spectrometer and is also powerfully utilised for THz and IR spectroscopic measurements. Figure 22(*a*) depicts the typical setup of the FTS. This system is based on a Michelson interfer-ometer. The interferometric signal between the transmitted and reflected waves divided by a beam splitter is digitised with an A/D converter and is computationally transformed into a frequency spectrum with the Fourier transform

(Figure 22(*b*)). The source is a broad-band emitter based on the blackbody radiation from thermal objects such as a halogen lamp and ceramic heater. As the detector, broad-band thermal detectors such as pyroelectric detectors and Si bolometers are typically used. A typical frequency spectrum taken by the FTS is shown in Figure 22(*b*). Compared to the THz-TDS, the FTS has an opposite feature in terms of the signal-to-noise ratio (S/N): this is reduced in the THz region, which is due to the fact that the intensity of the blackbody radiation is peaked at the mid-IR region and is substantially reduced in the higher frequency region.

As explained above, the two instruments have the com-plementary feature in terms of the S/N in frequency. There-fore, when researchers measure frequency spectra over a wide frequency region from IR to THz, they sometimes use both TDS and FTS and combine the two spectra obtained with the two instruments. As an example of such a combined measurement, IR and THz absorption spectra of CNT bun-dles are shown in [65]. Recently, the S/N of the TDS in a higher frequency region has been dramatically improved by use of another type of THz emitter. Matsubara et al. reported ultra-broad band TDS up to 200 THz by using air plasma induced by a 10 fs pulse laser [63]. Their technique enables time-resolved THz and IR spectroscopy over a very wide frequency range.

4.2. *Frequency-domain THz spectrometer (frequency-tunable THz emitter/detector)*

Though the TDS and FTS use highly sophisticated methods, these require an expensive femto-second pulse laser and
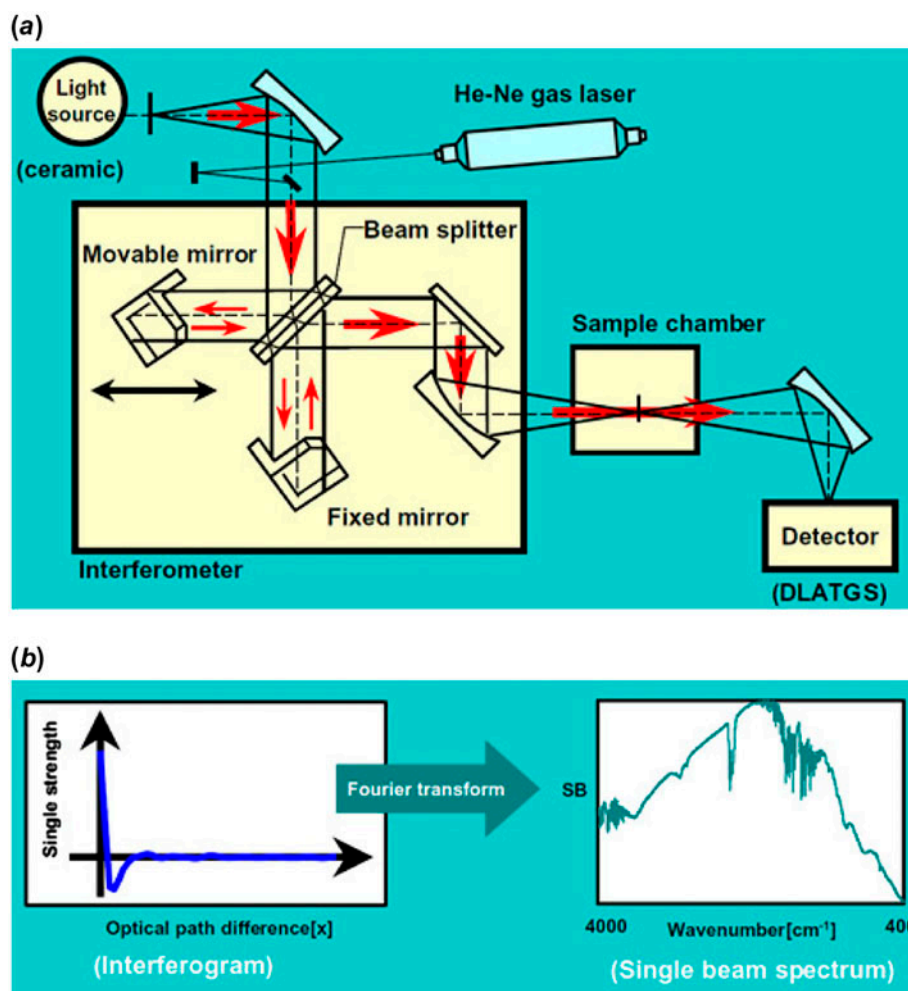
Figure 22. (*a*) Typical setup of the FTS system. (*b*) THz frequency spectrum taken with (*a*). Reproduced courtesy of JASCO Corporation.

a Michelson interferometer, respectively. Also these systems are based on broad-band THz emitters, which is another disadvantage in cases when THz measurements under frequency sweeping are needed. Alternative THz spectroscopic devices for allowing such a measurement are frequency-tunable THz emitters or detectors. In the past before the invention of the FTS and TDS, IR spectroscopy was performed using a frequency-tunable IR emitter with a diffraction grating. Nowadays there is a wide variety of more advanced frequency-tunable THz emitters including quantum cascade lasers [66], resonant tunnelling diodes [67], THz parametric oscillators [68], nonlinear photomixing of two IR or optical signals [69–72], backward-wave oscillators, Schottky diode multipliers, p-Ge hot-hole lasers [73,74], high-temperature superconducting THz emitters [75,76], etc.

Figure 23 depicts a setup of THz spectroscopy based on the nonlinear photomixing effect and displays an example of a THz spectrum taken with this method. The measurement

system consists of two IR lasers and a photomixer integrated with a Si lens for collimating the outgoing THz wave. The photomixer is irradiated with the two IR lasers whose frequency is slightly different from each other. As a result of the nonlinear effect of the photomixer, a beat signal corresponding to the frequency difference of the two IR lasers is generated and consequently continuous THz emission is radiated from the photomixer. The THz emission frequency is tunable by changing the frequency difference of the two IR lasers. The frequency band of the THz emission is determined by properties of the photomixer. For a standard semiconductor photomixer like GaAs, the maximum emission frequency is up to 2 THz and the emission intensity at 1 THz is 0.1–1 μW.

Instead there is THz spectroscopy with frequency-tunable THz detectors. Although THz detectors with frequency tunability remain to be fully explored, several types of frequency-tunable THz detectors have been developed: superconducting hot-electron mixers [77,78], 2DEG mixers
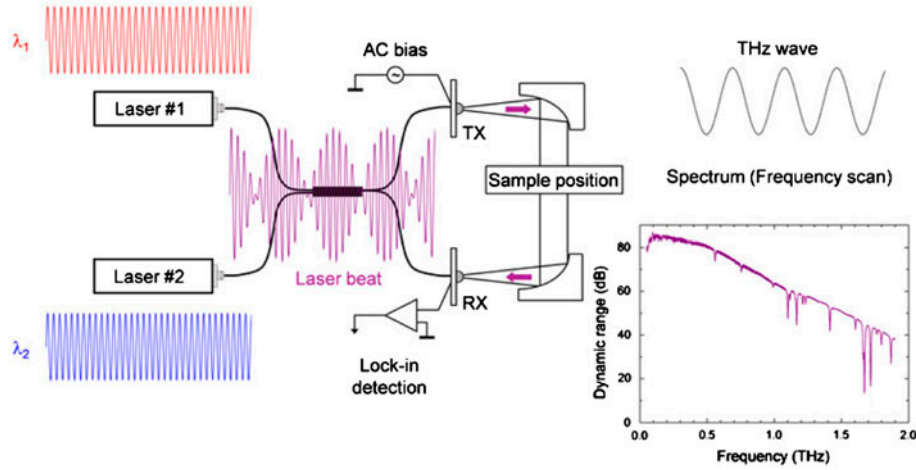
Figure 23. Sketch of the frequency-tunable THz emitter based on the nonlinear photomixing effect and THz frequency spectrum taken with this system. Reproduced courtesy of TOPTICA Photonics AG.
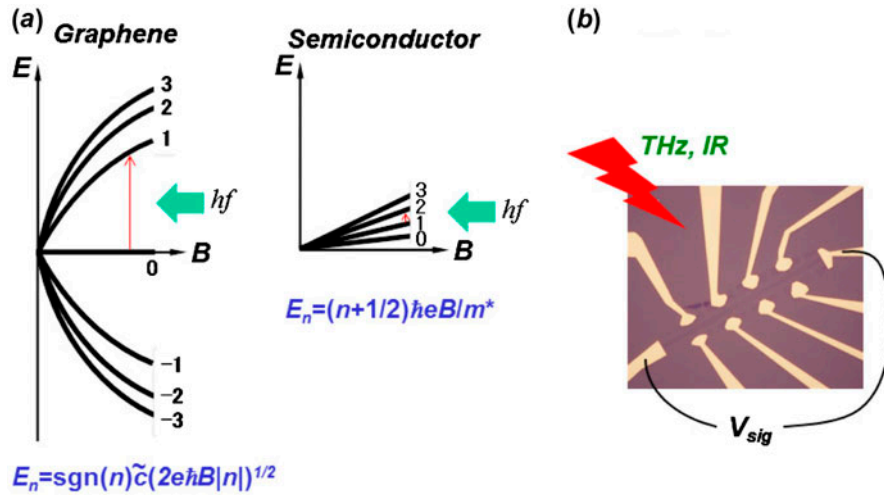

Figure 24. (*a*) Schematic representation of the LL density of states for the graphene (left) and the semiconductor (right). (*b*) Photograph of the graphene-based THz and IR spectrometer. Reprinted with permission from [80].

[79], 2DEG under magnetic field [62], CNT-QDs [7], etc. (See the Section 2.1 for details of the CNT-QD detector.)

4.3. Wide-band THz and IR spectrometer with graphene

The above frequency-tunable emitters and detectors have a problem that their emission and detection ranges are restricted to narrow frequency regions (below 5 THz). As a very wideband THz spectrometer based on a solid-state device, the use of graphene has been recently reported [80]. Its detectable frequency band ranges from the THz to the IR region (0.76–33 THz).

In the graphene material, carriers are regarded as massless Dirac fermions due to the linear dispersion relation [81, 82]. The THz and IR detection mechanism is based on the LL formation of Dirac fermions of the graphene under a

magnetic field and the resulting cyclotron resonance absorption of the electromagnetic waves. The LL for graphene is expressed as $E_n = \text{sgn}(n)\tilde{c}(2e\hbar B|n|)^{1/2}$ [83], which is in strong contrast to that for conventional semiconductors, $E_n = (n + 1/2)\hbar eB/m^*$. Here, n is the LL index, and $\tilde{c}$ is the effective carrier velocity. As explained in Section 2.2, the condition of the cyclotron resonance is that the photon energy, hf, of the incident electromagnetic wave matches the LL energy separation. Based on the above LL expressions, Figure 24(*a*) schematically compares the LL density of states between the graphene and the semiconductor. It is seen that the LL energy separation for the graphene is much larger than that for the semiconductor. Also the graphene has electron LLs and hole LLs that meet at the Dirac point, whereas electron LLs of the semiconductor are separated from hole LLs by the band gap energy (typically ∼eV).
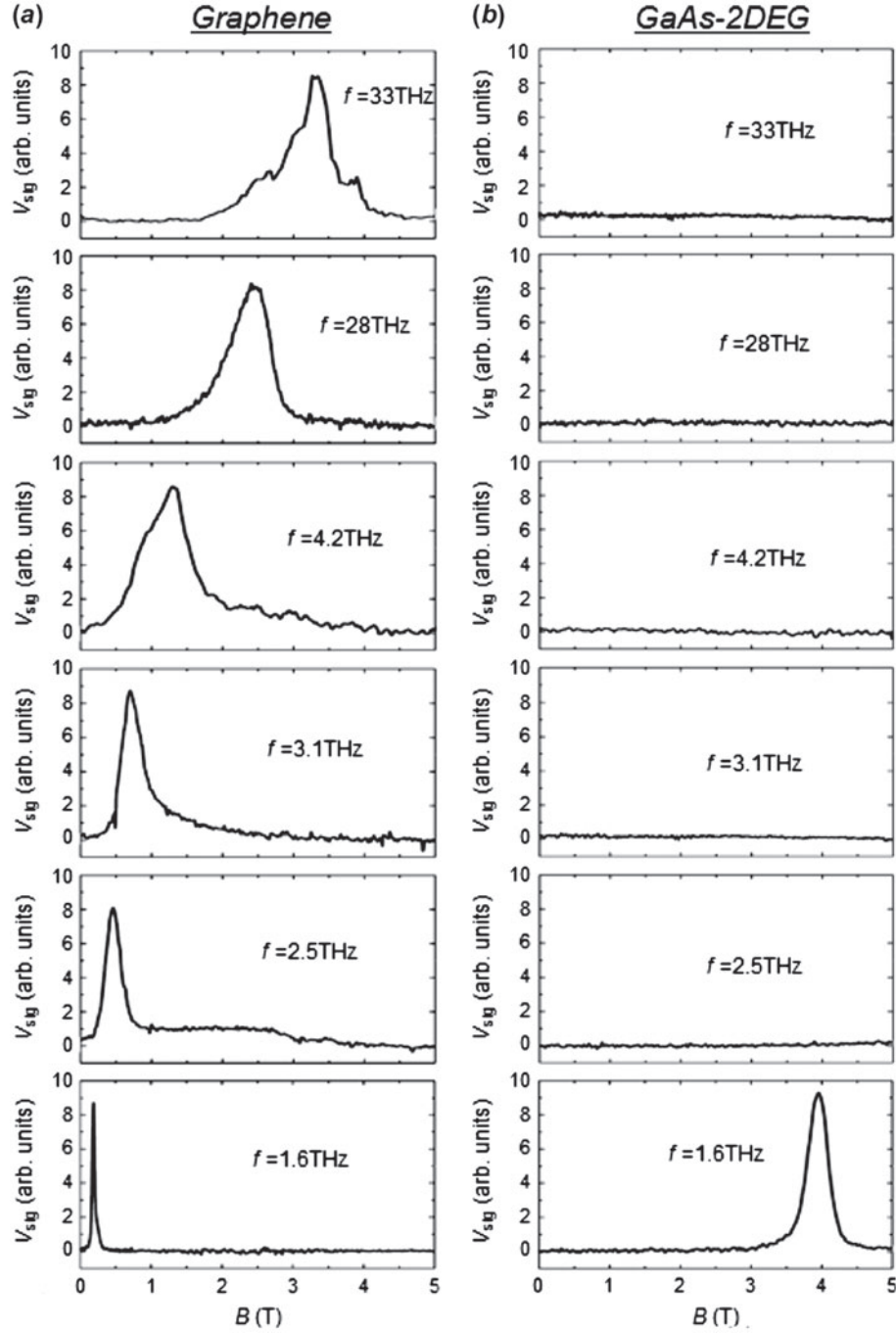
Figure 25. THz and IR detected signal V_{sig} as a function of magnetic field B at $f = 0.76$, 1.6, 2.5, 3.1, 4.2, 28, and 33 THz. (*a*) The graphene and (*b*) GaAs-2DEG are compared. Reprinted with permission from [80].

This unique feature makes the graphene device a magnetically frequency-tunable THz and IR detector over a very broad frequency range.

The photograph of Figure 24(*b*) depicts a graphene device used as the THz and IR detector. A single-layer graphene was exfoliated from a graphite and was attached on a SiO_2/Si

chip. The graphene device has current electrodes and a back-gate electrode. The graphene device was immersed into a 4.2 K cryostat and the magnetic field B was applied perpendicular to the graphene surface. As IR and THz illumination sources, a CO_2-gas IR laser ($f = 28$–33 THz) and a THz gas laser ($f = 0.76$–4.2 THz) were used. Voltage

changes, V_{sig}, with the THz/IR irradiation were measured using a lock-in amplifier, where the THz/IR waves were chopped at 24 Hz.

Figure 25 displays experimental results of the THz and IR response (detected signals V_{sig} versus B) for seven different frequencies of $f = 0.76, 1.6, 2.5, 3.1, 4.2, 28$, and 33 THz. For comparison, similar measurements were performed for the 2DEG on GaAs/AlGaAs. The data for the graphene reveal that the V_{sig} peaks appear for all the frequencies and that the peak position depends on the frequency. In contrast, the feature observed for the GaAs-2DEG is quite different. When $f = 0.76$ and 1.6 THz, the peak structures of V_{sig} were seen but their peak positions $B = 1.87$ and 3.96 T were distinct from $B = 0.042$ and 0.187 T for the graphene. Furthermore, for the GaAs-2DEG, there was no observable signal for higher frequencies than $f = 0.76$ and 1.6 THz.

These results can be ascribed to the large difference in the LL formation between the graphene and the semiconductor, as shown in Figure 24(*a*). When $B = 0$–5 T, the corresponding LL energy separation for the GaAs-2DEG is estimated to be 0–8.5 meV using the cyclotron effective mass of the GaAs crystal, $0.067m_0$ [19]. This energy range is insufficient to absorb the THz waves with higher photon energy than $hf = 8.5$ meV ($f = 2.1$ THz). This explains why the GaAs-2DEG device responds only to the THz wave with the lower photon energy $hf = 6.5$ meV and the lower frequencies $f = 0.76$ and 1.6 THz. For the graphene, on the other hand, the carriers are allowed to be excited in a much wider energy range. Taking into account the LL expression for the graphene and the effective carrier velocity ($\tilde{c} \sim 10^6$ m s^{-1}) [81], the observed THz and IR resonant detection is attributed to carrier excitation between the following LL indexes: $n = 1 \rightarrow 2$ for 0.76 THz, $n = 1 \rightarrow 2$ for 1.6 THz, $1 \rightarrow 2$ for 2.5 THz, $1 \rightarrow 2$ for 3.1 THz, $1 \rightarrow 2$ for 4.2 THz, $-1 \rightarrow 1$ for 28 THz, and $-1 \rightarrow 1$ for 33 THz.

The above results demonstrate that the graphene device works as a wide-band THz and IR spectrometer. The frequency range 0.76–33 THz is inaccessible via the earlier THz detectors with the superconductors [77,78], 2DEGs [62,79], and CNTs [7]. The detection bandwidth of the graphene-based spectrometer is potentially expected to be extended up to 100 THz.

5. Perspective of THz science and technology

In the long history of the study of the electromagnetic wave, the THz frequency region is the last frontier to be explored. Because of the great potential availability in a wide variety of fields, the academic and industrial impact will be immeasurable. Recent progress in nanotechnology and laser technology is greatly pushing the level of THz technology. In order to further explore and promote new THz science and technology, it is still critical to significantly enhance performance of elemental components such as source, detector, imaging and spectroscopy and to invent novel functional THz devices and instruments. For this purpose, new concepts and ideas will be required along with the extension of existing technologies.

In the field of basic sciences, new frontiers will be single-molecule THz imaging and spectroscopy, single THz-photon manipulation and correlation, astro-THz imaging for clarifying the birth of celestial bodies, etc. These subjects are quite challenging but intriguing. For these research directions, it will be necessary to make a breakthrough, such as the development of THz imaging with sub-10 nm resolution and on-demand single THz-photon source and detector.

Ultimate goals of industrial and medical applications are to realise high-capacity THz communication, high-resolution handy THz camera for safety and medical checks, biochemical THz examination, and so on.

I believe that these dreams will surely come true along with the evolution of materials, devices and lasers, and expect that new scientific findings and technologies obtained through the continuous effort of the THz research will have a large spillover effect on science, industry, and medicine.

Notes on contributor

Yukio Kawano is an associate professor of the Tokyo Institute of Technology. After receiving his Ph.D. degree in solid-state physics and engineering from the University of Tokyo in 2001, he worked as an assistant professor at the Department of Physics, University of Tokyo in 2001–2006 and as a Research Scientist at RIKEN during the period 2006–2011. His research interests include THz sensing, imaging and spectroscopy, scanning probe microscopy, and their applications to materials and biological research. Details of his research activity can be found at http://diana.pe.titech.ac.jp/kawano/eng/index.html.

References

[1] B. Ferguson, and X.-C. Zhang, *Materials for terahertz science and technology*, Nat. Mater. 1 (2002), pp. 26–33.
[2] M. Tonouchi, *Cutting-edge terahertz technology*, Nat. Photonics 1 (2007), pp. 97–105.
[3] D.F. Santavicca, M.O. Reese, A.B. True, C.A. Schmuttenmaer, and D.E. Prober, *Antenna-coupled niobium bolometers for terahertz spectroscopy*, IEEE Trans. Appl. Supercond. 17 (2007), p. 412.
[4] H. Takahashi, H. Shibai, M. Kawada, T. Hirao, T. Watabe, Y. Tsuduku, H. Nagata, H. Utsuno, Y. Hibi, S. Hirooka, T. Nakagawa, H. Kaneda, S. Matsuura, T. Kii, S.I. Makiuti, Y. Okamura, Y. Doi, H. Matsuo, N. Hiromoto, M. Fujiwara,

and M. Noda, *FIS: far-infrared surveyor on board ASTRO-F (IRIS)*, Proc. SPIE 4013 (2000), pp. 47–58.

[5] S.E. Church, M.J. Griffin, M.C. Price, P.A.R. Ade, R.J. Emery, and B.M. Swinyard, *Performance characteristics of doped-Ge photoconductors for the Infrared Space Observatory Long Wavelength Spectrometer*, Proc. SPIE 1946 (1993), pp. 116–125.

[6] S. Ariyoshi, C. Otani, A. Dobroiu, H. Matsuo, H. Sato, T. Taino, K. Kawase, and H. Shimizu, *Terahertz imaging with a direct detector based on superconducting tunnel junctions*, Appl. Phys. Lett. 88 (2006), 203503.

[7] Y. Kawano, T. Fuse, S. Toyokawa, T. Uchida, and K. Ishibashi, *Terahertz photon-assisted tunneling in carbon nanotube quantum dots*, J. Appl. Phys. 103 (2008), 034307.

[8] K. Shibata, A. Umeno, K.M. Cha, and K. Hirakawa, *Photon-assisted tunneling through self-assembled InAs quantum dots in the terahertz frequency range*, Phys. Rev. Lett. 109 (2012), 077401.

[9] P.K. Tien, and J.P. Gordon, *Multiphoton process observed in the interaction of microwave fields with the tunneling between superconductor films*, Phys. Rev. 129 (1963), pp. 647–651.

[10] As the general explanation of the photon-assisted tunneling, W.G. van der Wiel, T.H. Oosterkamp, S. de Franceschi, C.J.P.M. Harmans, and L.P. Kouwenhoven, *Photon assisted tunneling in quantum dots*, in *Strongly Correlated Fermions and Bosons in Low-Dimensional Disordered Systems*, I.V. Lerner, B.L. Althsuler, V.I. Fal'ko, and T. Giamarchi, eds., Kluwer Academic Publishers, Dordrecht, 2002, pp. 43–68.

[11] S. Komiyama, O. Astafiev, V. Antonov, H. Hirai, and T. Kutsuwa, *A single-photon detector in the far-infrared range*, Nature 403 (2000), pp. 405–407.

[12] J. Wei, D. Olaya, B.S. Karasik, S.V. Pereverzev, A.V. Sergeev, and M.E. Gershenson, *Ultrasensitive hot-electron nanobolometers for terahertz astrophysics*, Nat. Nanotechnol. 3 (2008), pp. 496–500.

[13] B.S. Karasik, A.V. Sergeev, and D.E. Prober, *Nanobolometers for THz photon detection*, IEEE Trans. Terahertz Sci. Technol. 1 (2011), pp. 97–111.

[14] Y. Kawano, T. Uchida, and K. Ishibashi, *Terahertz sensing with a carbon nanotube/two-dimensional electron gas hybrid transistor*, Appl. Phys. Lett. 95 (2009), 083123.

[15] R. Saito, G. Dresselhaus, and M.S. Dresselhaus, *Physical Properties of Carbon Nanotubes*, Imperial College Press, London, 1998.

[16] P.W. Barone, S. Baik, D.A. Heller, and M.S. Strano, *Near-infrared optical sensors based on single-walled carbon nanotubes*, Nat. Mater. 4 (2005), p. 86.

[17] M.E. Itkis, F. Borondics, A. Yu, and R.C. Haddon, *Bolometric infrared photoresponse of suspended single-walled carbon nanotube films*, Science 312 (2006), p. 413.

[18] K. Fu, R. Zannoni, C. Chan, S.H. Adams, J. Nicholson, E. Polizzi, and K.S. Yngvesson, *Terahertz detection in single wall carbon nanotubes*, Appl. Phys. Lett. 92 (2008), 033105.

[19] F. Thiele, U. Merkt, J.P. Kotthaus, G. Lommer, F. Malcher, U. Rossler, and G. Weimann, *Cyclotron masses in n-GaAs/Ga$_{1-x}$Al$_x$As heterojunctions*, Solid State Commun. 62 (1987), pp. 841–844.

[20] L. Crespi, T. Kodera, S. Oda, and Y. Kawano, *Terahertz radiation detection through a micro-scale antenna and a silicon-based quantum dot*, in Proceedings of 37th International Conference on Infrared, Millimeter, and Terahertz Waves, Wollongong, Australia, 2012.

[21] F. Miyamaru, M. Kamijyo, K. Takano, M. Hangyo, H. Miyazaki, and M.W. Takeda, *Characteristics and generation process of surface waves excited on a perfect conductor surface*, Opt. Express 18 (2010), 17576.

[22] M.A. Seo, H.R. Park, S.M. Koo, D.J. Park, J.H. Kang, O.K. Suwal, S.S. Choi, P.C.M. Planken, G.S. Park, N.K. Park, Q.H. Park, and D.S. Kim, *Terahertz field enhancement by a metallic nano slit operating beyond the skin-depth limit*, Nat. Photonics 3 (2009), pp. 152–156.

[23] D. Bozyigit, C. Lang, L. Steffen, J.M. Fink, C. Eichler, M. Baur, R. Bianchetti, P.J. Leek, S. Filipp, M.P. da Silva, A. Blais, and A. Wallraff, *Antibunching of microwave-frequency photons observed in correlation measurements using linear detectors, Nat*, Phys. 7 (2011), pp. 154–158.

[24] C. Eichler, D. Bozyigit, C. Lang, L. Steffen, J. Fink, and A. Wallraff, *Experimental state tomography of itinerant single microwave photons*, Phys. Rev. Lett. 106 (2011), 220503.

[25] Y. Kawano and S. Komiyama, *Spatial distribution of non-equilibrium electrons in quantum Hall devices: Imaging via cyclotron emission*, Phys. Rev. B 68 (2003), 085328.

[26] Y. Kawano and T. Okamoto, *Imaging of intra- and inter-Landau-level scattering in quantum Hall systems*, Phys. Rev. B 70 (2004), 081308(R).

[27] Y. Kawano and T. Okamoto, *Macroscopic channel-size effect of nonequilibrium electron distributions in quantum Hall conductors*, Phys. Rev. Lett. 95 (2005), 166801.

[28] J. Wakabayashi, and S. Kawaji, *Hall effect in silicon MOS inversion layers under strong magnetic fields*, J. Phys. Soc. Jpn. 44 (1978), pp. 1839–1849.

[29] S. Komiyama, Y. Kawaguchi, T. Osada, and Y. Shiraki, *Evidence of nonlocal breakdown of the integer quantum Hall effect*, Phys. Rev. Lett. 77 (1996), pp. 558–561.

[30] I.I. Kaya, G. Nachtwei, K. von Klitzing, and K. Eberl, *Spatially resolved monitoring of the evolution of the breakdown of the quantum Hall effect: Direct observation of inter-Landau-level tunneling*, Europhys. Lett. 46 (1999), pp. 62–67.

[31] S. Shikii, T. Kondo, M. Yamashita, M. Tonouchi, M. Hangyo, M. Tani, and K. Sakai, *Observation of supercurrent distribution in YBa$_2$Cu$_3$O$_{7-\delta}$ thin films using THz radiation excited with femtosecond laser pulses*, Appl. Phys. Lett. 74 (1999), pp. 1317–1319.

[32] N. Oda, *Uncooled bolometer-type Terahertz focal plane array and camera for real-time imaging*, C. R. Phys. 11 (2010), pp. 496–509.

[33] S. Boppel, A. Lisauskas, A. Max, V. Krozer, and H.G. Roskos, *CMOS detector arrays in a virtual 10-kilopixel camera for coherent terahertz real-time imaging*, Opt. Lett. 37 (2012), pp. 536–538.

[34] D.-T. Nguyen, F. Simoens, J.-L. Ouvrier-Buffet, J. Meilhan, J.-L. Coutaz, *Broadband THz uncooled antenna-coupled microbolometer array-electromagnetic design, simulations and measurements*, IEEE Trans. Terahertz, Sci. Technol. 2 (2012), 299.

[35] H. Hoshina, Y. Morisawa, H. Sato, A. Kamiya, I. Noda, Y. Ozaki, and C. Otani, *Higher order conformation of poly(3-hydroxyalkanoates) studied by terahertz time-domain spectroscopy*, Appl. Phys. Lett. 96 (2010), 101904.

[36] H. Hoshina, Y. Morisawa, H. Sato, H. Minamide, I. Noda, Y. Ozaki, and C. Otania, *Polarization and temperature dependent spectra of poly(3-hydroxyalkanoate)s measured at terahertz frequencies*, Phys. Chem. Chem. Phys. 13 (2011), pp. 9173–9179.

[37] M.A. Paesler and P.J. Moyer, *Near-field Optics*, Wiley, New York, 1996.

[38] M. Ohtsu (ed.), *Near-field Nano/Atom Optics and Technology*, Springer-Verlag, Berlin, 1998.

[39] E.H. Synge, *A suggested method for extending the microscopic resolution into the ultramicroscopic region*, Philos. Mag. 6 (1928), p. 356.

[40] E.A. Ash, and G. Nicholls, *Super resolution aperture scanning microscope*, Nature 23 (1972), p. 510.

[41] D.W. Pohl, W. Denk, and M. Lanz, *Optical stethoscopy: Image recording with resolution λ/20*, Appl. Phys. Lett. 44 (1984), p. 651.

[42] T. Saiki, S. Mononobe, M. Ohtsu, N. Saito, and J. Kusano, *Tailoring a high-transmission fiber probe for photon scanning tunneling microscope*, Appl. Phys. Lett. 68 (1996), pp. 2612–2614.

[43] F. Zenhausern, Y. Martin, and H.K. Wickramasinghe, *Scanning interferometric apertureless microscopy: optical imaging at 10 angstrom resolution*, Science 269 (1995), pp. 1083–1085.

[44] W.C. Symons III, K.W. Whites, and R.A. Lodder, *Theoretical and experimental characterization of a near-field scanning microwave microscope (NSMM)*, IEEE Trans. Microwave Theory Tech. 51 (2003), pp. 91–99.

[45] M. Tabib-Azar and Y. Wang, *Design and fabrication of scanning near-field microwave probes compatible with atomic force microscopy to image embedded nanostructures*, IEEE Trans. Microwave Theory Tech. 52 (2004), pp. 971–979.

[46] S. Hunsche, M. Koch, I. Brener, and M.C. Nuss, *THz near-field imaging*, Opt. Commun. 150 (1998), pp. 22–26.

[47] O. Mitrofanov, M. Lee, J.W.P. Hsu, I. Brener, R. Harel, J. Federici, J.D. Wynn, L.N. Pfeiffer, and K.W. West, *Collection-mode near-field imaging with 0.5-THz pulses*, IEEE J. Sel. Top. Quantum Electron. 7 (2001), pp. 600–607.

[48] R. Mueckstein, and O. Mitrofanov, *Imaging of terahertz surface plasmon waves excited on a gold surface by a focused beam*, Opt. Express 19 (2011), p. 3212.

[49] N. Klein, P. Lahl, U. Poppe, F. Kadlec, and P. Kužel, *A metal-dielectric antenna for terahertz near-field imaging*, J. Appl. Phys. 98 (2005), 014910.

[50] H.T. Chen, R. Kersting, and G.C. Cho, *Terahertz imaging with nanometer resolution*, Appl. Phys. Lett. 83 (2003), pp. 3009–3011.

[51] A.J. Huber, F. Keilmann, J. Wittborn, J. Aizpurua, and R. Hillenbrand, *Terahertz near-field nanoscopy of mobile carriers in single semiconductor nanodevices*, Nano Lett. 8 (2008), pp. 3766–3770.

[52] N.C.J. van der Valk and P.C.M. Planken, *Electro-optic detection of subwavelength terahertz spot sizes in the near field of a metal tip*, Appl. Phys. Lett. 81 (2002), pp. 1558–1560.

[53] T. Yuan, J.Z. Xu, and X.-C. Zhang, *Development of terahertz wave microscopes*, Infrared Phys. Technol. 45 (2004), pp. 417–425.

[54] R. Lecaque, S. Grésillon, N. Barbey, R. Peretti, J.-C. Rivoal, and C. Boccara, *THz near-field optical imaging by a local source*, Opt. Commun. 262 (2006), pp. 125–128.

[55] A. Doi, F. Blanchard, H. Hirori, and K. Tanaka, *Near-field THz imaging of free induction decay from a tyrosine crystal*, Opt. Express 18 (2010), pp. 18419–18424.

[56] J. Cunningham, M. Byrne, P. Upadhya, M. Lachab, E.H. Linfield, and A.G. Davies, *Terahertz evanescent field microscopy of dielectric materials using on-chip waveguides*, Appl. Phys. Lett. 92 (2008), 032903–1-3.

[57] Y. De Wilde, F. Formanek, R. Carminati, B. Gralak, P.-A. Lemoine, K. Joulain, J.-P. Mulet, Y. Chen, and J.-J. Greffet, *Thermal radiation scanning tunnelling microscopy*, Nature 444 (2006), pp. 740–743.

[58] Y. Kajihara, K. Kosaka, and S. Komiyama, *Thermally excited near-field radiation and far-field interference*, Opt. Express 19 (2011), p. 7695.

[59] Y. Kawano, and K. Ishibashi, *An on-chip near-field terahertz probe and detector*, Nat. Photonics 2 (2008), pp. 618–621.

[60] Y. Kawano, *Terahertz detectors: Quantum dots enable integrated terahertz imager*, Laser Focus World 45 (2009), 45–47&50.

[61] Y. Kawano and K. Ishibashi, *On-chip near-field terahertz detection based on a two-dimensional electron gas*, Physica E 42 (2010), pp. 1188–1191.

[62] D. Suzuki, S. Oda, and Y. Kawano, *GaAs/AlGaAs field-effect transistor for tunable terahertz detection and spectroscopy with built-in signal modulation*, Appl. Phys. Lett. 102 (2013), 122102.

[63] E. Matsubara, M. Nagai, and M. Ashida, *Ultrabroadband coherent electric field from far infrared to 200 THz using air plasma induced by 10 fs pulses*, Appl. Phys. Lett. 101 (2012), 011105.

[64] As a review of the THz-TDS, for example, C.A. Schmuttenmaer, *Exploring dynamics in the far-infrared with terahertz spectroscopy*, Chem. Rev. 104 (2004), pp. 1759–1779.

[65] Q. Zhang, L. Ren, E.H. Hároz, T. Arikawa, C.L. Pint, F. Mirri, R.H. Hauge, and J. Kono, *Origin of the terahertz absorption peak in single-walled carbon nanotubes*, Proceedings of 36th International Conference on Infrared, Millimeter and Terahertz Waves (IRMMW-THz), Houston TX, 2011.

[66] B.S. Williams, *Terahertz quantum-cascade lasers*, Nat. Photonics 1 (2007), p. 517.

[67] S. Suzuki, M. Asada, A. Teranishi, H. Sugiyama, and H. Yokoyama, *Fundamental oscillation of resonant tunneling diodes above 1 THz at room temperature*, Appl. Phys. Lett. 97 (2010), p. 242102.

[68] K. Kawase, J. Shikata, and H. Ito, *Terahertz wave parametric source*, J. Phys. D: Appl. Phys. 35 (2002), p. R1.

[69] S. Verghese, K.A. McIntosh, and E.R. Brown, *Optical and terahertz power limits in the low-temperature-grown GaAs photomixers*, Appl. Phys. Lett. 71 (1997), p. 2743.

[70] H. Ito, T. Furuta, F. Nakajima, K. Yoshino, and T. Ishibashi, *Photonic generation of continuous THz wave using uni-traveling-carrier photodiode*, J. Lightwave Technol. 23 (2005), p. 4016.

[71] M. Tang, H. Minamide, Y. Wang, T. Notake, S. Ohno, and H. Ito, *Tunable terahertz-wave generation from DAST crystal pumped by a monolithic dual-wavelength fiber laser*, Opt. Express 19 (2011), pp. 779–786.

[72] S. Preu, G.H. Döhler, S. Malzer, L.J. Wang, and A.C. Gossard, *Tunable, continuous-wave Terahertz photomixer sources and applications*, J. Appl. Phys. 109 (2011), p. 061301.

[73] S. Komiyama, *Far-infrared emission from population-inverted hot-carrier system in p-Ge*, Phys. Rev. Lett. 48 (1982), pp. 271–297.

[74] A.A. Andronov, *Hot-electrons in semiconductors and submillimeter waves*, Sov. Phys. Semicond. 21 (1987), p. 701.

[75] L. Ozyuzer, A.E. Koshelev, C. Kurter, N. Gopalsami, Q. Li, M. Tachiki, K. Kadowaki, T. Yamamoto, H. Minami, H. Yamaguchi, T. Tachiki, K.E. Gray, W.-K. Kwok, and U. Welp, *Emission of coherent THz radiation from superconductors*, Science 318 (2007), p. 1291.

[76] M. Tsujimoto, T. Yamamoto, K. Delfanazari, R. Nakayama, T. Kitamura, M. Sawamura, T. Kashiwagi, H. Minami, M. Tachiki, K. Kadowaki, and R.A. Klemm, *Broadly tunable subterahertz emission from internal branches of the current-voltage characteristics of superconducting Bi₂Sr₂CaCu₂O₈₊δ single crystals*, Phys. Rev. Lett. 108 (2012), p. 107006.

[77] A.D. Semenov, H.-W. Hübers, H. Richter, M. Birk, M. Krocka, U. Mair, Y.B. Vachtomin, M.I. Finkel, S.V. Antipov, B.M. Voronov, K.V. Smirnov, N.S. Kaurova, V.N. Drakinski, and G.N. Gol'tsman, *Superconducting hot-electron bolometer mixer for terahertz heterodyne receivers*, IEEE Trans. Appl. Supercond. 13 (2003), pp. 168–171.

[78] W. Zhang, P. Khosropanah, J.R. Gao, E.L. Kollberg, K.S. Yngvesson, T. Bansal, R. Barends, and T.M. Klapwijk, *Quantum noise in a terahertz hot electron bolometer mixer*, Appl. Phys. Lett. 96 (2010), 111113.

[79] K.S. Yngvesson, *Ultrafast two-dimensional electron gas detector and mixer for terahertz radiation*, Appl. Phys. Lett. 76 (2000), pp. 777–779.

[80] Y. Kawano, *Wide-band frequency-tunable terahertz and infrared detection with graphene*, Nanotechnology 24 (2013), 214004.

[81] K.S. Novoselov, A.K. Geim, S.V. Morozov, D. Jiang, M.I. Katsnelson, I.V. Grigorieva, S.V. Dubonos, and A.A. Firsov, *Two-dimensional gas of massless Dirac fermions in graphene*, Nature 438 (2005), p. 197.

[82] Y. Zhang, Y.-W. Tan, H.L. Stormer, and P. Kim, *Experimental observation of the quantum Hall effect and Berry's phase in graphene*, Nature 438 (2005), p. 201.

[83] J.W. McClure, *Diamagnetism of graphite*, Phys. Rev. 104 (1956), p. 666.